THE V471 TAURI SYSTEM: A MULTI-DATA-TYPE PROBE

T. R. VACCARO[1], R. E. WILSON[2,3], W. VAN HAMME[4], AND DIRK TERRELL[5]

[1] Department of Physics and Astronomy, St. Cloud State University, St. Cloud, MN 56301, USA; trvaccaro@gmail.com
[2] Astronomy Department, University of Florida, Gainesville, FL 32611, USA; rewilson@ufl.edu
[3] Astronomy Department, Indiana University, Swain Hall West, Bloomington, IN 47405, USA
[4] Department of Physics, Florida International University, Miami, FL 33199, USA; vanhamme@fiu.edu
[5] Department of Space Studies, Southwest Research Institute, 1050 Walnut Street, Suite 300, Boulder, CO 80302, USA; terrell@boulder.swri.edu

ABSTRACT

V471 Tauri, a white dwarf–red dwarf eclipsing binary (EB) in the Hyades, is well known for stimulating development of common envelope theory, whereby novae and other cataclysmic variables form from much wider binaries by catastrophic orbit shrinkage. Our evaluation of a recent imaging search that reported negative results for a much postulated third body shows that the object could have escaped detection or may have actually been seen. The balance of evidence continues to favor a brown dwarf companion about 12 AU from the EB. A recently developed algorithm finds unified solutions from three data types. New radial velocities (RVs) of the red dwarf and $BVR_C I_C$ light curves are solved simultaneously along with white dwarf and red dwarf RVs from the literature, *uvby* data, the *Microvariability and Oscillations of Stars* mission light curve, and 40 years of eclipse timings. Precision-based weighting is the key to proper information balance among the various data sets. Timewise variation of modeled starspots allows unified solution of multiple data eras. Light-curve amplitudes strongly suggest decreasing spottedness from 1976 to about 1980, followed by approximately constant spot coverage from 1981 to 2005. An explanation is proposed for lack of noticeable variation in 1981 light curves, in terms of competition between spot and tidal variations. Photometric–spectroscopic distance is estimated. The red dwarf mass comes out larger than normal for a K2 V star, and even larger than adopted in several structure and evolution papers. An identified cause for this result is that much improved red dwarf RV curves now exist.

Key words: binaries: eclipsing – binaries: spectroscopic – stars: individual (V471 Tau)

Supporting material: machine-readable tables

1. INTRODUCTION

V471 Tau, a white dwarf–red dwarf eclipsing binary (EB) in the Hyades with orbit period 0.52118 days, is primarily known for its unique historical role as a stimulus to common envelope evolution theory (Chau et al. 1974; Refsdal et al. 1974; Sparks & Stecher 1974; Alexander et al. 1976; Ostriker 1976; Paczynski 1976; Taam et al. 1978). Other properties include a likely brown dwarf companion to the EB, measured white dwarf spin, mass loss and exchange in a detached binary, differential rotation measured via magnetic spots, spot distributions, accurate white dwarf parameters, and photometric–spectroscopic distance measures that help to pin down the binary's location within the Hyades. Publications on its properties and evolution include the discovery paper and follow-up (Nelson & Young 1970, 1976), along with many that form the background for this paper. O'Brien et al. (2001, hereafter OBBS) have interesting discussions of evolutionary possibilities, including ideas that would involve a third star. Reasonable space limitations restrict our discussions to those most directly related to the putative third object's orbital properties, along with relative and absolute properties of the EB. Issues beyond the scope of this paper include radio eclipses (Lim et al. 1996; Nicholls & Storey 1999), red dwarf atmospheric structure (Kim & Walter 1998; Walter 2004), chemical abundances (Martin et al. 1997; Still & Hussain 2003; Garcia-Alvarez et al. 2005; Shimansky et al. 2011), a circumbinary shell (Sion et al. 1989), red dwarf wind (Mullan et al. 1989), and flares (Young et al. 1983; Tunca et al. 1993).

Physical/geometric quantities are derived here by simultaneous analysis of radial velocity (RV) curves, differential and absolute light curves,[6] and eclipse timings by a unified multi-data-type algorithm (Wilson & Van Hamme 2014) that allows all of the main sources of orbital, stellar, and timing information to be analyzed coherently and is built around a general binary star model.

V471 Tau has been widely believed to show a subtle light-time variation due to the EB's motion about the barycenter of a postulated triple system (hereafter 3b system). The semi-amplitude is about 2.3 minutes over an orbital period of 30+ yr. Guinan & Ribas (2001) analyzed the variation from 163 eclipse timings, finding that the third object's mass corresponds to a brown dwarf for inclinations (i_{3b}) above about 35°. Here the presumed 3b companion's properties are estimated, based on three types of data solved simultaneously in several combinations and also separately—6 RV curves, 9 light curves, and 224 eclipse timings. Results of our analysis, together with a history of interpretations of timing residual excursions, are given in Section 5.

Hierarchical multiple systems are fairly common despite the difficulties of discovery due to long periods, small light-time amplitudes, and faintness of companions (Pribulla & Rucinski 2006; Rucinski et al. 2007). Guinan & Ribas (2001) proposed (their Section 5) to observe the EB's astrometric orbit due to its reflex motion about a triple-system barycenter (thus measuring the outer orbit's inclination and the 3b system's dynamical mass) and also proposed coronographic

---

[6] Here "absolute" refers to observed and computed fluxes being in standard physical units. The definition extends to light curves that can reliably be converted to absolute flux, such as those in accurately calibrated standard magnitudes.

imaging to detect the 3b. They included evolution-based estimates of the suspected brown dwarf's magnitude and orbit-based estimates of its maximum angular distance from the EB in their text and their Table 2 and Figure 2. Although the astrometry has not yet begun, an adaptive optics (AO) image from 2014 December 11 by Hardy et al. (2015) has led to a claim that the 3b's existence has been disproved. Our analyses indicate that the 3b has several ways to have avoided detection. We estimate significantly fainter minimum brightness for the 3b than did Hardy et al., with our result based on more extensive data than previously accessed in any V471 Tau analyses. Specifics are discussed in Section 9. We also show that its expected location is closer to the AO image center (i.e., closer to the EB) than estimated by Hardy et al. (2015). At least two features at the revised angular distance, in their image of the field, could be candidates for the long-sought object.

2. OBSERVATIONAL INPUT

RVs of the red dwarf from our 1998 Kitt Peak National Observatory (KPNO) observations made with the 0.9 m Coudé Feed of the 2.1 m telescope are in Table 1. Their characteristics (instrument, integration times, etc.) are in Vaccaro & Wilson (2002). Other red star RVs by Young (1976), Bois et al. (1988), Hussain et al. (2006), and Kaminski et al. (2007)[7] also were utilized, along with white dwarf RVs by OBBS. The five sets of red star RVs are in approximate mutual agreement according to visual inspection within their scatter bands. Four of the twelve white dwarf RVs from the *Hubble Space Telescope* tabulated by OBBS preceded NASA's Corrective Optics Space Telescope Axial Replacement (COSTAR) repair mission. Here the eight OBBS post-COSTAR RVs were used, but not the four pre-COSTAR RVs (see OBBS for comments on the relative merits of their pre- and post-COSTAR data).

The white dwarf Si IV RVs illustrated in Figure 6 of Sion et al. (2012) were not fully analyzed here, partly because the physical situation in which the lines are formed is excessively complicated, and partly because the RVs lead to an implausible red star mass. The physical intricacy is made clear by Sion et al.'s Section 4, which discusses irregular surface distributions combined with line strength modulations on the 555 s white dwarf rotation period, as well as blending of absorption- and emission-line components and blending of unresolved Zeeman components. Funneling of accretion flows into the magnetic poles also can be expected. Accordingly, the measured RVs are not likely to be representative of the white dwarf surface as a whole, although they may be formed on or near the surface. Measurements on Sion et al.'s Figure 6 show that the white dwarf RV amplitude is 28% larger than in OBBS, necessarily leading to a greater binary system mass, according to Kepler's third law, and to a greater mass ratio (M_2/M_1) so that the red star's share of the total mass is increased over that in OBBS. A least-squares solution, based on the figure's dots and all red star RVs, quantified this expectation by finding a red star mass of 1.68 $M_\odot$, which we do not consider realistic for a K2 V star. Although the idea of using these lines was resourceful, the implausible RV amplitude probably indicates that the local physics is too uncertain for extraction of reliable masses.

Our 1998 BVR_CI_C differential light curves with respect to comparison star BD +16°515, observed at KPNO with the 0.9 m Southeastern Association for Research in Astronomy telescope and described in Vaccaro & Wilson (2002), are in Table 2. Means and standard deviations of 31 newly observed BVR_CI_C magnitudes of BD +16°515 are in Table 3. Band-to-band changes of eclipse depth are dramatic, as seen in Figures 1–9. Also entered were *uvby* light curves by Rucinski (1981) and an unusually extensive one from the *Microvariability and Oscillations of Stars* (*MOST*) mission (Kaminski et al. 2007). In order to keep (iterated) solution run times within reasonable limits, normal points of the 57,000+ *MOST* light-curve points were made by averaging times and magnitudes in groups of 10 points, except for those in the steep descending and ascending parts of eclipses where no averaging was done. This procedure resulted in the 6001 normal points used here and shown in Figure 9. Standard errors of averages were calculated from standard errors of individual observations. Normal point weights (inversely proportional to normal point standard errors squared) were used as individual weights in all our solutions that included the *MOST* light curve. The *MOST* differential magnitudes had 9.5 mag added (by us) to simulate actual magnitudes, which improved initial solution convergence. The additive constant does not affect results since solutions are given with luminosity ratios, $L_1/(L_1 + L_2)$, rather than L_1 and L_2.

Eclipse minima (total 224) from many observers were entered into our unified light-RV-timing solutions, most having been collected and tabulated by Ibanoglu et al. (2005). A few that are not in the Ibanoglu et al. online table are in Table 4, including four recent ones by Hardy et al. (2015).

To derive ephemerides on a steady time system, and following a suggestion by Bastian (2000), Guinan & Ribas (2001) consistently adopted HJED, an astronomical helio-centric version of universal Atomic Time,[8] and later authors of V471 Tau timing analyses have also done so. Differences between HJED and Coordinated Universal Time (UTC), which essentially tracks Earth's decelerating rotation, have accumulated to somewhat over 1 minute during the past four decades and obviously need to be considered in investigations of a 2.3 minute effect. All times for observations utilized in this paper have been converted to HJED or were originally reported in HJED.

3. PROCEDURAL OVERVIEW

Unified binary system solutions, as the term is used here, simultaneously process RVs, multiband light curves, and eclipse timings so as to treat stellar, orbital, and ephemeris parameters coherently in one conceptual step.[9] The solutions are by the well-known method of differential corrections (DC), as implemented in Wilson & Devinney (1971) and revised several times, most recently as described in Wilson & Van Hamme (2014). Such solutions allow all considered astrophysical effects to be handled without personal intervention, except for choice of starting estimates. Although the development in Wilson & Van Hamme (2014) emphasizes the orbit period (P), a reference time, and other timing-related quantities

---

[7]   The HJED times in Table 1 of Kaminski et al. (2007) have mid-exposure corrections that are full rather than the appropriate half integration times, according to K. Kaminski, who kindly provided the properly corrected times used in this paper.

[8]   See Sections B6 and B7 of the Astronomical Almanac for the Year 2013 (Gallaudet & Robinson 2012).
[9]   If necessary, the full parameter set can be broken into subsets to handle discontinuous period changes, although that was not done here.

Table 1
Red Dwarf 1998 Radial Velocities

HJD	HJED	RV (km s^{-1})	Error (km s^{-1})	HJD	HJED	RV (km s^{-1})	Error (km s^{-1})	HJD	HJED	RV (km s^{-1})	Error (km s^{-1})
2451115.74334	2451115.74407	150.75	2.43	2451119.97287	2451119.97360	71.80	2.86	2451123.94066	2451123.94139	101.86	3.08
2451115.76646	2451115.76720	127.03	3.36	2451119.99392	2451119.99465	29.40	3.51	2451123.96675	2451123.96748	142.83	2.48
2451115.80814	2451115.80887	67.28	3.76	2451120.69401	2451120.69474	−86.62	3.68	2451123.98779	2451123.98852	166.47	3.48
2451115.82916	2451115.82989	17.70	4.71	2451120.71505	2451120.71578	−63.05	3.37	2451124.00883	2451124.00956	179.75	3.01
2451115.85965	2451115.86038	−34.01	2.68	2451120.73609	2451120.73682	−18.14	3.31	2451124.67755	2451124.67828	41.20	2.82
2451115.88069	2451115.88142	−62.08	3.57	2451120.76867	2451120.76940	36.50	2.33	2451124.69859	2451124.69933	8.17	2.72
2451115.90463	2451115.90536	−91.47	3.47	2451120.78972	2451120.79045	72.97	3.26	2451124.71965	2451124.72038	−32.14	3.13
2451115.92567	2451115.92640	−104.07	2.54	2451120.81076	2451120.81149	105.76	2.91	2451124.74071	2451124.74144	−67.55	4.62
2451115.94671	2451115.94745	−121.51	4.56	2451120.83180	2451120.83253	129.20	2.90	2451124.76902	2451124.76976	−101.68	3.23
2451115.97263	2451115.97336	−115.26	4.21	2451120.85942	2451120.86015	160.30	3.67	2451124.79041	2451124.79114	−116.14	3.74
2451115.99366	2451115.99439	−90.57	2.21	2451120.88047	2451120.88120	180.57	2.25	2451124.81163	2451124.81236	−117.86	3.38
2451117.72782	2451117.72855	162.68	4.13	2451120.90150	2451120.90223	183.59	2.43	2451124.83267	2451124.83340	−112.96	2.84
2451117.75008	2451117.75081	177.66	3.20	2451120.93026	2451120.93099	177.45	3.82	2451124.85370	2451124.85443	−95.83	2.97
2451117.77166	2451117.77240	177.51	4.10	2451120.95131	2451120.95204	157.39	2.73	2451124.87474	2451124.87548	−72.88	2.69
2451117.79334	2451117.79408	174.68	2.96	2451120.97235	2451120.97308	133.49	2.33	2451124.89750	2451124.89823	−36.92	2.81
2451117.82558	2451117.82632	153.90	2.90	2451120.99339	2451120.99412	106.38	2.57	2451124.91853	2451124.91926	1.59	2.48
2451117.84533	2451117.84606	134.35	2.33	2451121.01774	2451121.01847	70.74	3.95	2451124.93956	2451124.94029	36.96	2.56
2451118.70485	2451118.70558	73.23	2.26	2451121.69333	2451121.69406	−116.54	3.27	2451124.96061	2451124.96135	72.47	3.76
2451118.73872	2451118.73945	119.48	1.86	2451121.72619	2451121.72692	−99.96	2.44	2451124.98164	2451124.98238	102.90	2.03
2451118.75977	2451118.76050	146.35	3.02	2451121.75320	2451121.75394	−65.87	2.86	2451125.00268	2451125.00341	136.19	2.65
2451118.80495	2451118.80568	186.83	1.82	2451121.77425	2451121.77498	−25.82	3.08	2451125.02912	2451125.02985	166.97	3.26
2451118.83388	2451118.83461	179.38	3.00	2451121.79528	2451121.79601	7.29	1.77	2451125.67631	2451125.67704	120.26	2.60
2451118.85516	2451118.85589	168.58	2.16	2451121.81632	2451121.81705	42.97	3.03	2451125.69736	2451125.69809	89.11	4.06
2451118.87621	2451118.87694	150.92	3.76	2451121.85086	2451121.85159	101.58	2.76	2451125.71840	2451125.71913	52.17	3.87
2451118.89896	2451118.89969	124.91	2.72	2451121.87269	2451121.87342	129.19	1.92	2451125.73943	2451125.74016	8.11	2.36
2451118.92000	2451118.92073	90.37	2.09	2451121.89372	2451121.89445	156.94	2.74	2451125.77829	2451125.77903	−61.57	4.18
2451118.94103	2451118.94176	53.01	2.94	2451121.91477	2451121.91550	178.24	2.27	2451125.79933	2451125.80006	−91.21	3.46
2451118.96209	2451118.96282	11.96	3.53	2451121.93584	2451121.93657	180.96	2.82	2451125.82038	2451125.82111	−107.14	2.62
2451118.98479	2451118.98552	−32.13	2.29	2451121.96619	2451121.96692	176.30	3.64	2451125.84144	2451125.84218	−118.25	3.47
2451119.00760	2451119.00833	−69.95	4.08	2451121.99232	2451121.99305	158.11	2.73	2451125.86539	2451125.86612	−115.76	2.93
2451119.70071	2451119.70144	−7.77	3.07	2451122.01363	2451122.01436	140.11	2.49	2451125.88834	2451125.88907	−104.00	3.16
2451119.72174	2451119.72247	27.63	4.15	2451123.68673	2451123.68746	−52.03	3.88	2451125.91125	2451125.91198	−78.14	2.51
2451119.74277	2451119.74350	61.31	2.51	2451123.70781	2451123.70854	−82.69	3.43	2451125.93230	2451125.93303	−48.05	3.15
2451119.76382	2451119.76455	95.76	3.67	2451123.72884	2451123.72957	−102.70	2.48	2451125.95336	2451125.95409	−14.92	2.43
2451119.79115	2451119.79189	135.49	3.52	2451123.74988	2451123.75061	−110.56	3.13	2451125.98089	2451125.98162	36.66	2.24
2451119.81218	2451119.81292	156.45	3.11	2451123.77711	2451123.77784	−116.17	2.46	2451126.00221	2451126.00294	67.12	3.65
2451119.83323	2451119.83396	178.16	2.17	2451123.79814	2451123.79888	−106.79	2.66	2451126.02324	2451126.02397	106.17	2.77
2451119.85427	2451119.85500	179.75	3.63	2451123.83267	2451123.83340	−68.75	3.69	2451126.68505	2451126.68578	158.59	3.37
2451119.88811	2451119.88884	170.94	2.99	2451123.85431	2451123.85505	−37.82	1.91	2451126.70609	2451126.70682	134.94	1.78
2451119.90916	2451119.90989	158.35	3.00	2451123.87544	2451123.87617	−0.19	2.61	2451126.73635	2451126.73708	90.36	2.26
2451119.93020	2451119.93093	133.01	2.83	2451123.89651	2451123.89725	39.15	3.68	2451126.78502	2451126.78575	−4.84	2.77
2451119.95124	2451119.95197	101.90	2.86	2451123.91765	2451123.91838	74.56	3.50	2451126.80638	2451126.80712	−39.00	2.73

Note. Errors are individual RV standard errors.

(This table is available in machine-readable form.)

Table 2
$BVR_C I_C$ 1998 Light Curves

HJD	HJED	Δm_B	HJD	HJED	Δm_V	HJD	HJED	Δm_{R_C}	HJD	HJED	Δm_{I_C}
2451115.82767	2451115.82840	−0.347	2451115.82530	2451115.82603	−0.027	2451115.81963	2451115.82036	0.159	2451115.82234	2451115.82307	0.425
2451115.82989	2451115.83062	−0.345	2451115.82643	2451115.82716	−0.026	2451115.82155	2451115.82228	0.163	2451115.82317	2451115.82390	0.427
2451115.87319	2451115.87392	−0.339	2451115.87142	2451115.87215	−0.017	2451115.86929	2451115.87002	0.174	2451115.82400	2451115.82473	0.427
2451115.93012	2451115.93085	−0.375	2451115.92841	2451115.92914	−0.053	2451115.87038	2451115.87111	0.175	2451115.85564	2451115.85637	0.433
2451115.93806	2451115.93879	−0.379	2451115.93350	2451115.93423	−0.057	2451115.92742	2451115.92815	0.139	2451115.85623	2451115.85696	0.435

Note. Differential magnitudes are in the sense *Variable–Comparison*, with BD +16°515 as the comparison star.

(This table is available in its entirety in machine-readable form.)

Table 3
Comparison Star BD +16°515 Standard Magnitudes

Band	Magnitude
B	10.718 ± 0.011
V	9.433 ± 0.011
R_C	8.803 ± 0.026
I_C	8.246 ± 0.019

Note. The mean HJED of 31 observations in each band is 2,456,337.2525, ranging from 2,456,328.6090 to 2,456,350.6354.

(dP/dt, $d\omega/dt$,[10] and light-time effect parameters), any chosen model parameters can be processed as a coherent set with optional automated data weighting. Table 5 summarizes the data sets used in this paper and includes the time window for each.

3.1. Data Weighting Basics

The essentials of light-curve weighting are in Wilson (1979), including curve-dependent, level-dependent, and individual data point weights. Weighting is important in simultaneous solutions of multiple data sets, especially when several data types are included, but can be somewhat tedious if done by personal intervention, so it varies among publications and often is not mentioned. Without proper weighting the weakest observations are likely to have the most influence. RV weighting and eclipse timing weighting are not level dependent but otherwise are done in the same way as light-curve weighting. Only weight ratios matter among the points of a given data subset such as a light or RV curve, since curve-dependent weights are computed subsequently by DC, taking account of individual weights. Accordingly, the scaling factor for individual weights is arbitrary and was set to unity. Level-dependent weights are generated within DC from applicable statistics that were assumed to be photon counting statistics for the light curves.

3.2. Curve-dependent Weights for V471 Tau

Iterative automation of curve-dependent weights is briefly outlined and applied to several EBs in Wilson & Van Hamme (2014), and a full explanation is in the documentation monograph that accompanies the DC program's most recent version.[11] Automated weighting saves an operational step for each input curve and also eliminates a class of possible mistakes, such as entry of a σ from individual data points when averages of points were the actual input. Our intention was to apply automated curve-dependent weights in the V471 Tau solutions. However, it became clear that stretches of the light curves show systematic deviations from modeled curves due to unknown, possibly transient effects. These anomalous intervals lead to oversized σ's that can significantly misrepresent a curve's precision. Accordingly, weights were not based on automated curve-dependent σ's, but on fixed σ's (Table 6) found separately for each light curve by Fourier series fits (up to 7θ), excluding points near eclipse of the white dwarf. These standard deviations served as the (fixed) curve-dependent light-

curve σ's for all solutions. For the RVs and timings, the σ's are from RV-only and timing-only DC solutions, respectively.

3.3. Treatment of Magnetic Spot Growth and Decay

At most epochs, spottedness is the largest cause of V471 Tau's brightness variation for wavelengths longer than about 0.4 μm and cannot be ignored, although the red dwarf's tidal variation is significant, with reflection being a much smaller effect. Eclipse depths increase strongly toward short wavelengths and are the largest cause of variation in the ultraviolet, although of course restricted to a small phase range, leaving variation due to spots usually being dominant over the rest of the cycle. Dark magnetic spots are common on stars that have well-developed outer convection zones, and especially on rapid rotators. Because very close binary components typically have been tidally dragged into co-rotation with the (fast) orbital motion, spot activity due to magnetic fields that are generated by convective motions and advective flows can be far more extensive on short-period binaries than on the Sun. The spots may densely cover large regions, although not being individually much larger than their solar counterparts (Rucinski 1979).

Because the spots come and go, they can be problematic for light-curve solutions that cover long stretches of time. Onset and disappearance times may need to be considered carefully where data sets extend for long times and where they overlap or nearly overlap in time. The conceptual spots[12] can be varied in area by setting start and stop times and assigning times of maximum size. Even where input data eras are well separated in time, the start–stop facility for spots is essential for allowing individual curves to be fitted within a common overall data set (i.e., since real spots come and go, model spots must come and go). Considerable experimentation may be needed to attain approximate representations of spots or spotted regions. If the trial experiments essentially succeed, an impersonal algorithm can refine locations and maximum sizes, as well as time markers for growth and decay. V471 Tau solutions require parameters for many conceptual spots in addition to the other parameters (3 spots per epoch × 3 epochs = 9 adjusted spots), yet iterations involving parameter subsets ensured good convergence. A recent scheme for improved accuracy in spot representation (Wilson 2012) was applied. In the interest of simplicity, the modeled timewise profile is, in general, an asymmetric trapezoid, with a symmetric trapezoid or triangle as special cases. Results are in Table 7.

Doppler imaging, also known as eclipse mapping (e.g., Vogt 1987; Vogt et al. 1987), is based on spectral line profiles and gives far more detailed spot information than the light curves now at hand, so one cannot expect to learn much about V471 Tau's spot behavior beyond that in Ramseyer et al. (1995) and Hussain et al. (2006). However, photometry is more readily done in quantity than is spectroscopy, so its usefulness for spots could improve significantly if a tradition developed whereby light curves were published rather than only illustrated. About 15 other whole light curves (counting multiband data observed together as one curve) have been illustrated in papers and could have helped to fill timewise gaps if they had been published.[13] There was some success in attempts to obtain such observations that

---

[10] Parameter $d\omega/dt$ is the rotation rate of an elliptical orbit within its own plane.
[11] Available via FTP download at ftp://ftp.astro.ufl.edu/pub/wilson/lcdc2015/

---

[12] Here the expression "conceptual spots" refers to the option of regarding a model spot as representing either an individual spot or a spotted area.
[13] See comments on the importance of publishing observations in useful form by D. Helfand, posted at http://aas.org/posts/news/2013/06/presidents-column-making-excellent-journals-even-better.
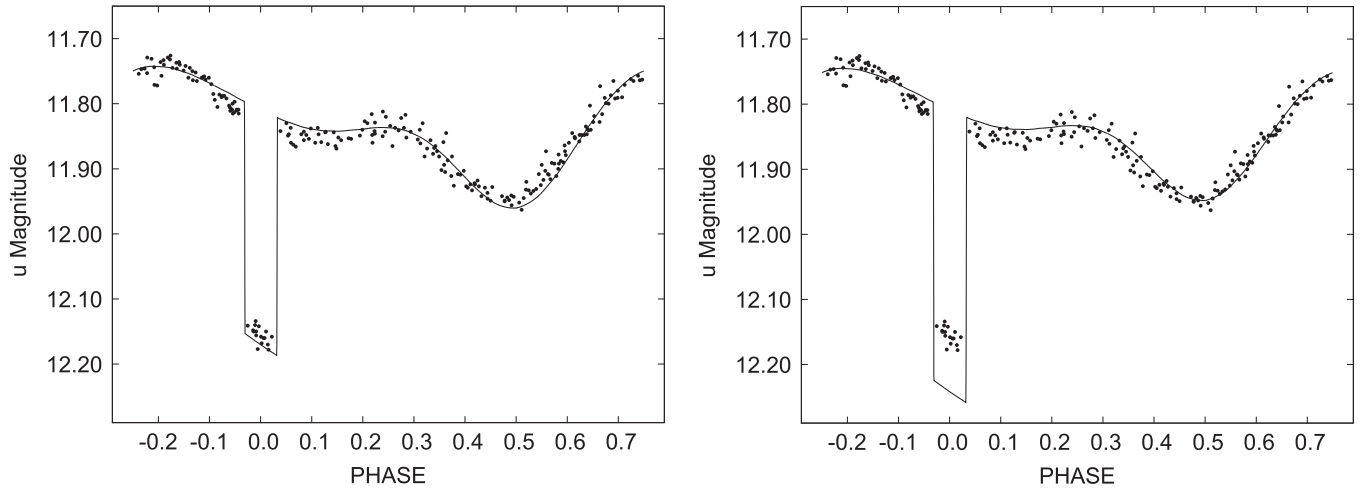
Figure 1. V471 Tau phased *u*-band data of 1976 November–December by Rucinski (1981) with solution curves. The left and right panels are based on the All Data Excluding *MOST* solution (Table 8, second column) and the All Data Excluding *MOST* with *MOST*-fixed-radii solution (Table 8, fifth column) parameters, respectively. Variation due to spots is largest here among this paper's analyzed epochs.
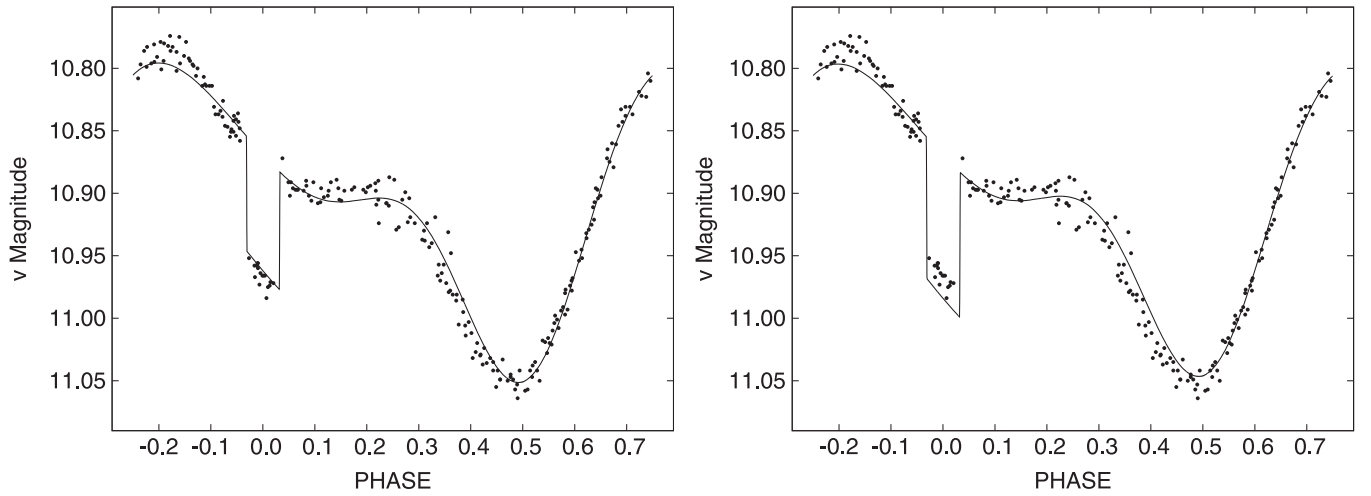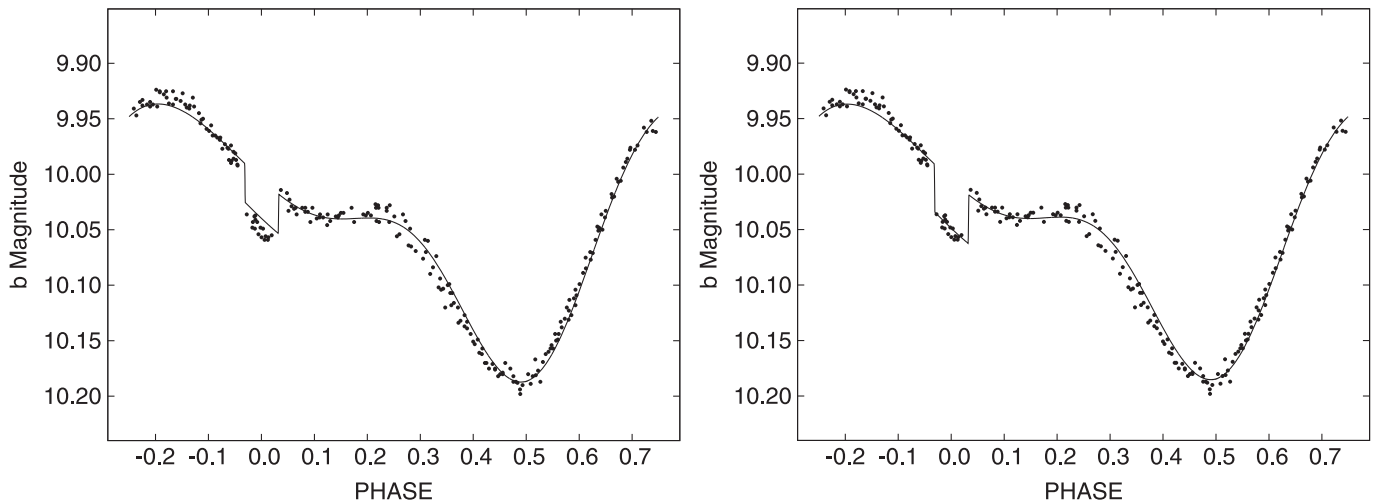

Figure 2. Same as Figure 1, but for the *v* band.

Figure 3. Same as Figure 1, but for the *b* band.
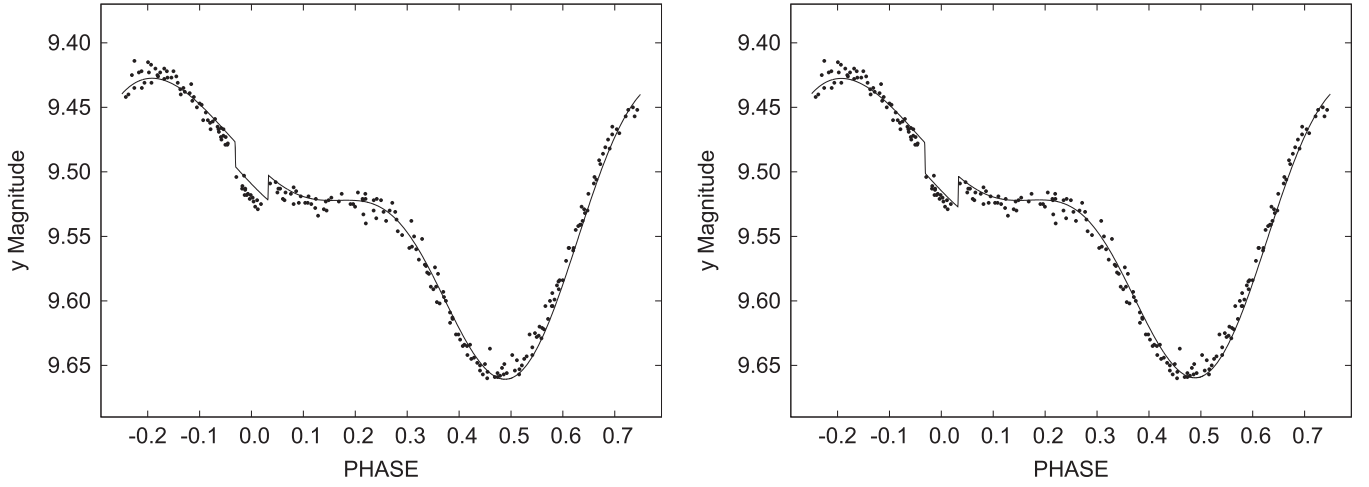
Figure 4. Same as Figure 1, but for the *y* band.
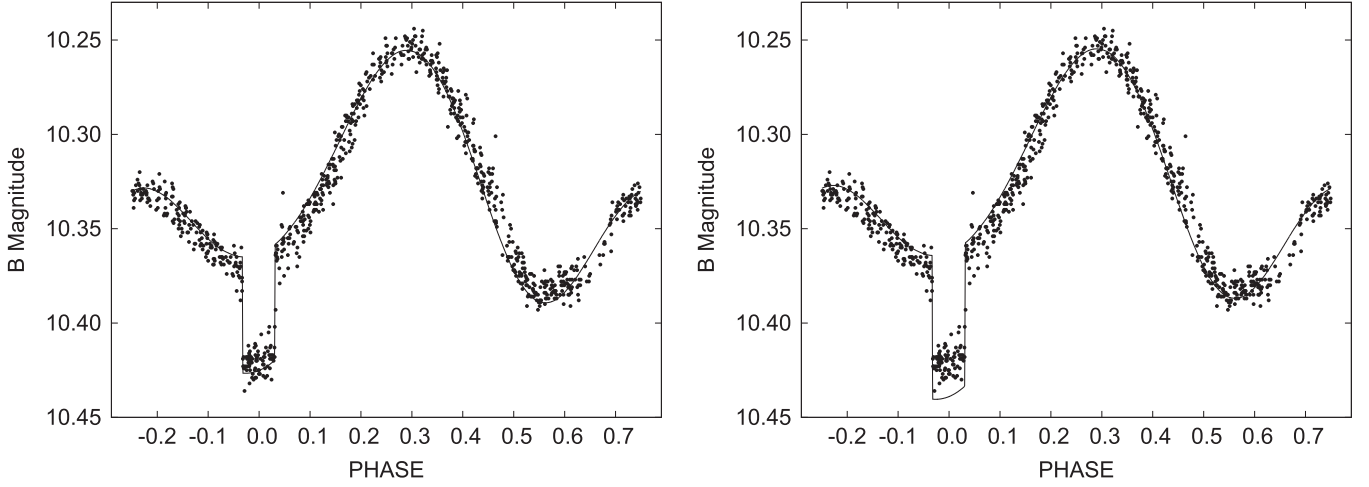
Figure 5. Same as Figure 1, but for the 1998 November *B*-band observations of this paper. Note that the amplitude is much smaller than in the 1976 October–November observations of Figures 1–4, allowing for the difference in vertical scales.
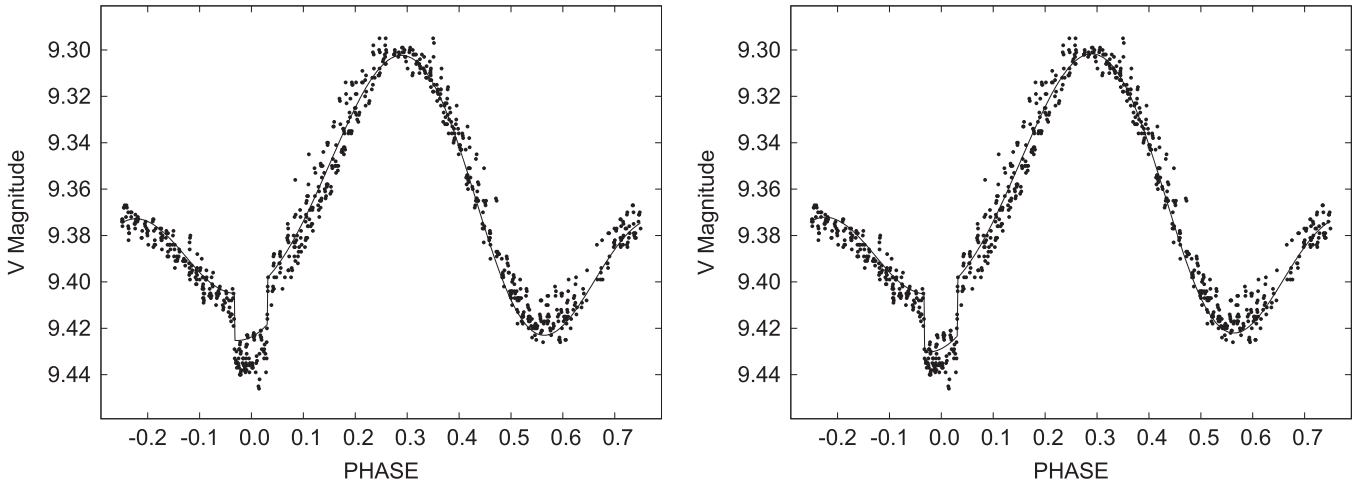
Figure 6. Same as Figure 1, but for the *V*-band observations of this paper.

added one RV curve and one light curve to our database (see acknowledgments).

The parameters for a given spot are:

1. spot center "latitude" (0 at the +*z* pole, π radians at the −*z* pole);

2. spot center longitude (0 to 2π rad, starting from the binary system line of centers, increasing counterclockwise as seen from above the +*z* pole);

3. spot angular radius at the time of maximum size (in rad), defined at the star center;
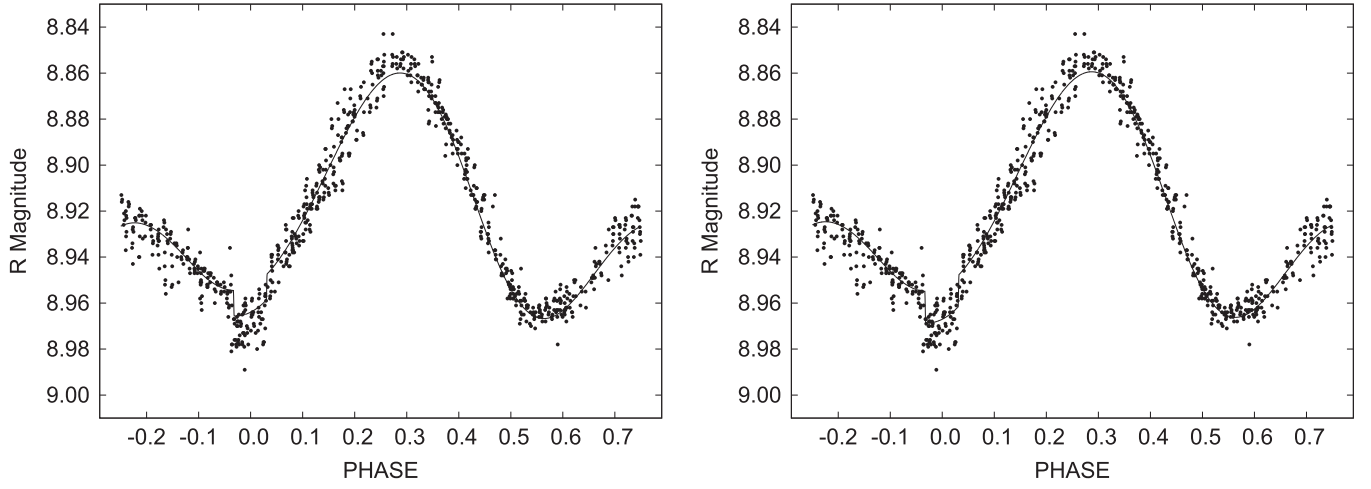
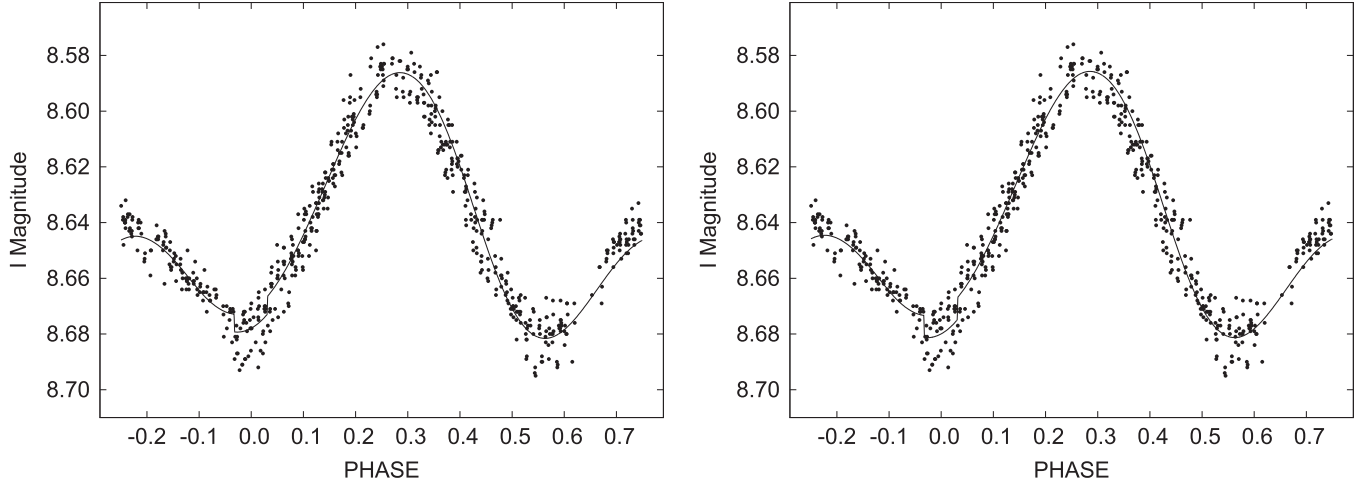**Figure 7.** Same as Figure 1, but for the R_C-band observations of this paper.

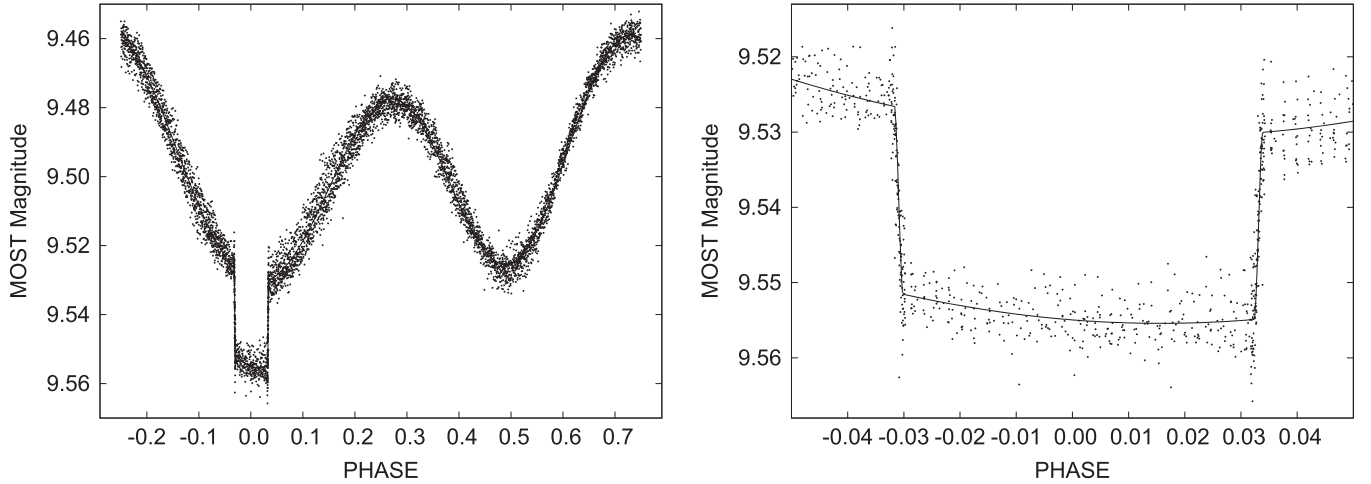**Figure 8.** Same as Figure 1, but for the I_C-band observations of this paper.

Figure 9. *MOST* observations of 2005 December by Kaminski et al. (2007) phased with the ephemeris of the light-curve-only solution (column 4 of Table 8). Variation due to spots is much smaller than in 1976 or 1998. The points are the light-curve data processed in our solutions. They are averages of 10 original points, except in the very brief partial eclipse phases, where they are original points. The right panel shows the eclipse in more detail.

4. ratio of local spot temperature to underlying (i.e., no-spot) local temperature;

5. spot appearance time (and start time of linear growth in area);

6. ending time of area growth (and start time of constant area);

7. ending time of constant area (and start time of linear area decay);

Table 4
Eclipse Timings Not in Table 1 of Ibanoglu et al. (2005)

Timing (HJED)	References	Timing (HJED)	References	Timing (HJED)	References
2443053.89343	(1)	2446006.91705	(2)	2454810.22895	(4)
2443113.82994	(1)	2446025.67955	(2)	2454884.23699	(4)
2443485.95520	(1)	2446798.59438	(3)	2455064.56636	(4)
2444195.80596	(1)	2446823.61126	(3)	2455075.51140	(4)
2444226.55528	(1)	2454028.45413	(4)	2455076.55364	(4)
2445671.79622	(2)	2454055.55555	(4)	2455512.78406	(5)
2455532.58899	(5)	2454055.61859	(5)	2455547.70336	(5)

References. (1) Miranda et al. (2007). (2) Beach (1985). (3) Eitter (1987). (4) Hric et al. (2011); (5) Hardy et al. (2015).

8. spot disappearance time;
9. ratio of spot angular drift rate to mean orbital angular revolution rate on star 1; and
10. ratio of spot angular drift rate to mean orbital angular revolution rate on star 2.

The last two parameters were set to unity so the spots stay at fixed longitudes on the synchronously rotating red dwarf. The start and ending times for constant spot area were taken to coincide with the start and ending times of the corresponding light curves.

3.4. Fractional Spot Coverage over Recent Decades

The last column of Table 7 is fractional spot area for the entire surface, which declined from 13% for the 1976 Rucinski (1981) observations, to 10% for our 1998 KPNO observations, and to 1.7% for the 2005 Kaminski et al. (2007) MOST observations. The red dwarf may have cyclic spot activity similar to the Sun's, although neither periodicity nor timewise trends can be established from just three epochs. Naturally periodic spot behavior could cause cyclic variations of small amplitude in the eclipse timing residuals (see Section 8). So is there really a trend in total spot coverage, or is too much being read from just three points? If there is a trend, is its form simple (say, linear or bilinear) or more complicated? A natural plan is to examine light-curve amplitude versus time, which requires many more epochs than the three for which digital light curves are available, with amplitude as a rough proxy for total spot coverage. All of the light-curve papers that lacked the actual observations *did* have light-curve plots whose amplitudes could be measured graphically. The references are Cester & Pucillo (1976), Tunca et al. (1979, 1993), Skillman & Patterson (1988), Ibanoglu et al. (2005), and Miranda et al. (2007). There are more light-curve epochs than papers because some authors observed at more than one epoch. Of course, amplitudes from papers that did contain or had online digital light curves (Rucinski 1981; Kaminski et al. 2007) and from this paper also were measured. Utilization of those light curves involved computation of theoretical light curves corresponding to the spot parameters in Table 7 and reading of their amplitudes, which are plotted along with the graphically determined amplitudes in Figure 10. The left panel has only bands that are close to V in effective wavelength (V, y, and MOST)—those most abundant in the literature—while the right panel has all bands. For the left panel there should be little concern with possible band dependence of amplitude since the MOST effective wavelength is near 5250 Å, so not very far from V and y. A related issue concerns how strongly amplitude varies from band to band. The theoretical light curves

mentioned above show that the band dependence is modest compared to observational scatter in the observed curves. The right panel, with amplitudes for all reasonably standard bands, helps by having 31 observed and 9 analytic points, compared to the 17 observed and 3 analytic points of the left panel. The overall inference reinforces the trend seen in spot coverage, which is represented by only three points, and shows that it is not a linear trend by filling timewise gaps. Instead, an interval of fast decline is followed by one of nearly constant amplitude. One must keep in mind that the variation is not entirely due to spots but has a significant tidal component. Note that the computational points at a given epoch fall rather close to corresponding graphical points, giving confidence in consistency of the overall process.

3.5. Curious 1981 October Light Curves: A Proposed Explanation

Figures 11 and 12 illustrate 1981 October uvby light curves of V471 Tau (Rucinski 1983) that look basically level and flat. Although only 11 points are in each band, the points are about as well distributed in phase as can be expected and show little or no variation except for one point in each band that lies within the eclipse of the white dwarf. Rucinski's Figure 1 shows, in addition to y-band points, an idealized rendition of a y light curve from 5 yr earlier that has an amplitude of about 0.20 mag. The substantial variation seen in the 1976 observations obviously disappeared in 1981. Can the absence of variation in 1981 be due to absence of spots? One must consider that tidal (i.e., ellipsoidal) variation of the red dwarf is surely present since, with the system parameters (star masses, sizes, etc.) being well known, the tidal variation can be computed reliably from well-established equipotential theory. Computations show the tidal amplitude to be of order 0.1 mag, although band dependent, which should readily be seen in the light curves, so complete absence of spots should leave a pure tidal variation, not an essentially flat curve. Furthermore, given that spots had been the dominant cause of brightness variation, from system discovery until about 1980, their complete vanishing would be a major surprise. No suggestion of a reason for the 1981 curves' lack of variation seems to have been published, but there is a simple possibility—that the surface spot distribution was just that needed to cancel the ellipsoidal effect. A few numerical trials, followed by a simultaneous uvby solution of the 44 Rucinski (1983) points, quickly found a spot configuration that approximately satisfies our conjecture. However, the actual uvby fits showed a somewhat complicated result whereby the impersonal least-squares solution exploited phase gaps (again—only 11 points per band) to weave among the dots with appreciable nonzero

Table 5
V471 Tau Data Sets

Reference	Data Type	Time Range (JD)	Number of Points	Calendar Range
Rucinski (1981)	*u*, *v*, *b*, *y* lc's	2443076-2443085	232, 237, 237, 237	1976 Oct–Nov
This paper	*B*, *V*, R_C, I_C lc's	2451115-2451127	876, 850, 798, 643	1998 Oct–Nov
Kaminski et al. (2007)	*MOST* lc	2453708-2453718	6001[a]	2005 Dec
O'Brien et al. (2001)	RV1	2449643-2449651	7	1994 Oct
O'Brien et al. (2001)	RV1	2449792.9	1	1995 Mar
Young (1976)	RV2	2440517-2441283	37	1969 Oct–1971 Nov
Bois et al. (1988)	RV2	2442797-2445648	202	1976 Jan–1983 Nov
This paper	RV2	2451115-2451127	126	1998 Oct–Nov
Hussain et al. (2006)	RV2	2452601-2452605	93	2002 Nov
Kaminski et al. (2007)	RV2	2453717-2453724	37	2005 Dec
Ibanoglu et al. (2005); Table 4	Eclipse Timings	2440612-2455547	224	1970 Jan–2010 Dec

Note.
[a] Normal points; see comment in Section 2.

Table 6
Curve-dependent σ's

Curve	σ
RV1	1.70 km s^{-1}
RV2	2.00 km s^{-1}
u	0.205×10^{-6}
v	0.349×10^{-6}
b	0.517×10^{-6}
y	0.794×10^{-6}
B	0.419×10^{-6}
V	1.04×10^{-6}
R_C	1.67×10^{-6}
I_C	1.95×10^{-6}
MOST normals	0.484×10^{-6}
Timings	0.000175 days

Table 7
Spot Parameters

Co-latitude (rad)	Longitude (rad)	Radius (rad)	$T_{spot}/T2$	Fractional Spot Area
0.632	0.021	0.514	0.779	0.065
2.352	5.128	0.222	0.903	0.012
0.582	1.888	0.448	0.853	0.049
0.471	4.101	0.355	0.798	0.031
2.342	2.405	0.373	0.930	0.035
2.132	5.636	0.391	0.879	0.038
0.329	1.705	0.223	0.599	0.012
0.575	3.549	0.117	0.727	0.003
2.040	0.165	0.053	0.988	0.001

Note. The first three spots are for epochs HJED 2,442,076 to 2,444,086, with maximum spot radii between HJED 2,443,076 and HJED 2,443,086, the observational window for the Rucinski (1981) light curves. The second triad of spots is for epochs HJED 2,450,115–2,452,127, with maximum spot radiii between HJED 2,451,115 and 2,451,127 (the KPNO observational window). The last triad is for epochs HJED 2,452,713–2,454,724, with the spots reaching maximum radii between HJED 2,453,713 and 2,453,724 (the *MOST* observational window). Spot parameters are defined in Section 3.3.

variation. Accordingly, the apparent lack of variation in 1981 seems to be mainly due to a temporary spot distribution that nearly cancels ellipsoidal variation, combined with overall low spottedness. A contributing factor is the small number of data points, with inevitable phase gaps that make eye assessments difficult. The analytic *y*-band amplitude is ≈0.04 mag, and a corresponding point is in both panels of Figure 10 at JD 2,444,892. Figures 11 and 12 also contain the fitted curves and theoretical pure tidal curves (i.e., without spots).

4. SOLUTIONS: CHARACTER AND OUTCOME

Only about 10^{-4} of the red dwarf's face can be eclipsed by the white dwarf, so only one eclipse per orbit cycle is realistically observable—a nearly rectangular notch as the very hot white dwarf is occulted by the red star. The notch is increasingly prominent toward short wavelengths and nearly disappears in the red and infrared bands. The partial phases last only ≈1% of an eclipse, so, even at the best time resolution to date, they measure little more than the length of the projected chord traversed by the partially occulted white dwarf. A consequence is near degeneracy between the dimensionless white dwarf radius, R_1/a, and EB orbit inclination, *i*. Although the solutions directly or indirectly accessed ≈60,000 light-curve points, the radii remain a problem owing to the nearly rectangular eclipse form that compromises the inclination's accuracy, and thereby that of R_1/a and R_2/a. For given *i*, the partial phase duration essentially measures $(R_2 - R_1)/a$, while the full eclipse width, again for given *i*, basically measures the sum of the relative radii, $(R_1 + R_2)/a$. The sum and difference together determine R_1/a and R_2/a. Because the ratio R_1/R_2 is very small (of order 0.01), the eclipse duration is affected only slightly by R_1/a, so the white dwarf radius can be nearly lost in the noise. Actual radii R_1 and R_2 are further affected by the *a* versus *i* correlation. The red star's slight tidal and rotational distortions are properly computed and should not cause significant uncertainty. In the 3b orbit, only the product $a_{3b} \sin i_{3b}$ is measurable, not a_{3b} and i_{3b} separately, since none of the input data can distinguish outer orbit inclination effects from those of outer orbit size.

4.1. Solution Results

Both absolute (Wilson 2008) and traditional solutions were carried out. Briefly the distinction is that absolute solutions have their observed and computed fluxes in standard physical units. Naturally only absolute solutions can produce distance as a direct solution output, with a standard error. Rucinski's *uvby* light curves can be put on an absolute flux basis reliably, since he provided all the necessary information. They were processed
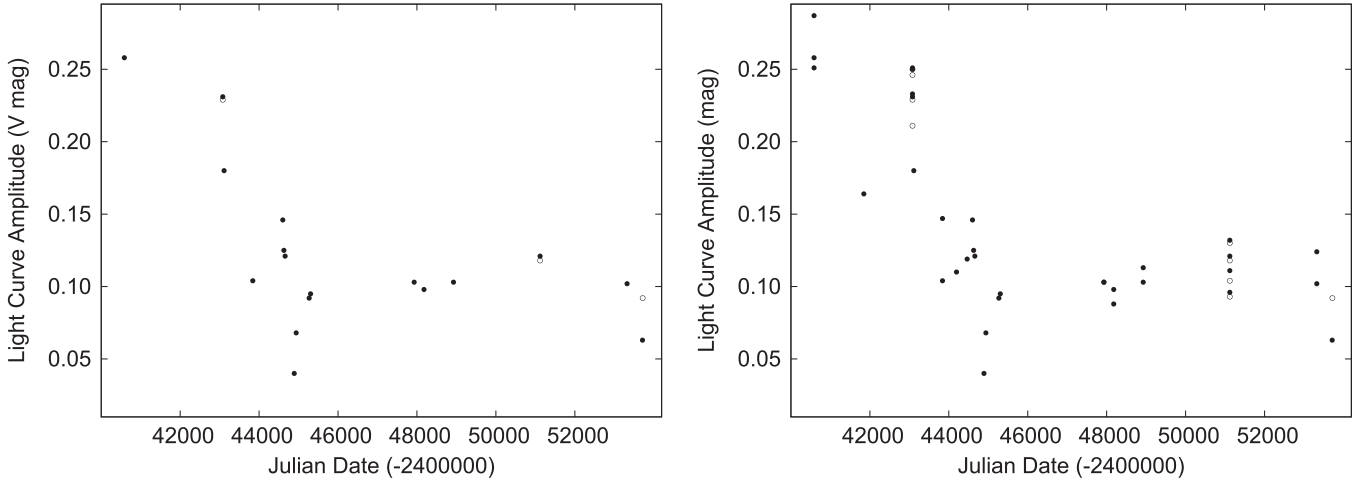
Figure 10. Light-curve amplitude vs. time over recent decades, showing decline that was not simply linear but a fast decline followed by an era of near constancy. Left panel: amplitude vs. time for *V*, *y*, and *MOST* mission light curves, which have similar effective wavelengths. The main variation phenomena are modulation by starspots and tides, both being on the red dwarf. Dots are observed amplitudes read from light-curve figures (mostly from the literature, with a few from our 1998 KPNO observations). Open circles are analytic amplitudes that correspond to our solution parameters. Right panel: same as in the left panel, but for all bands (*u*, *v*, *b*, *y*, *B*, *V*, R_C, I_C, *MOST*).
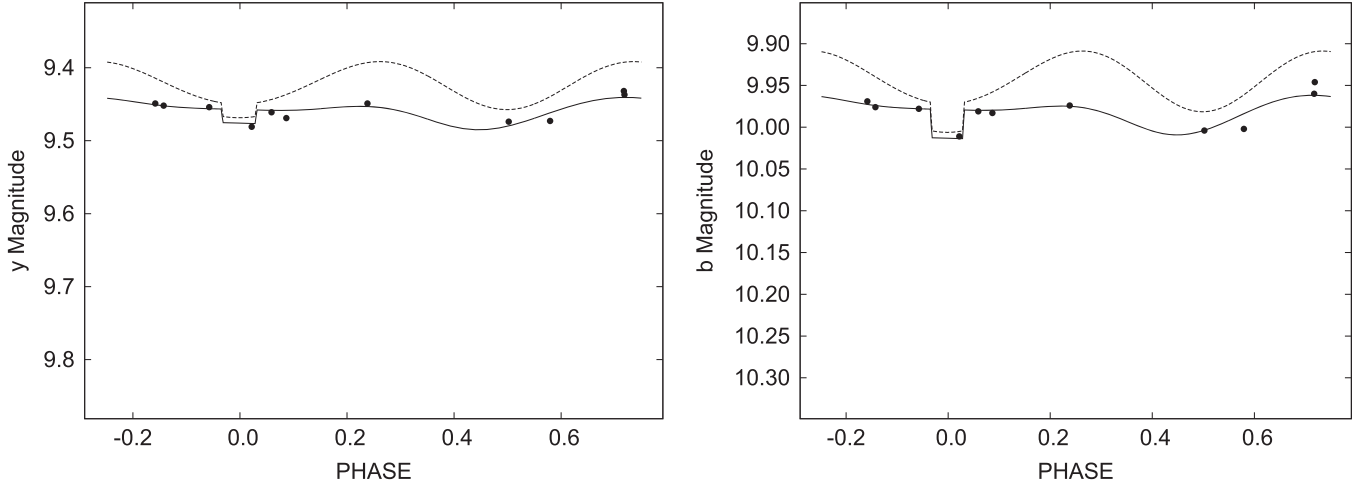
Figure 11. Results showing that a curious flat light curve of 1981 can be explained by partial cancelation between tidal and spot variation. Left panel: *y* light curve by Rucinski (1983) (dots) with remarkably little variation, as mentioned by Rucinski and discussed in Section 3.5. The lower curve is from a least-squares solution that followed exploration of spot configurations that nearly cancel variation due to tides. The upper curve is for complete absence of starspots, so with only tidal distortion and a small reflection effect outside eclipse. The large amount of white space allows the *u*, *v*, *b*, and *y* panels (see also next figure) to have the same differential magnitude scale, so as to allow direct comparison of amplitudes. Right panel: same as left panel, but for the Rucinski (1983) *b* curve.
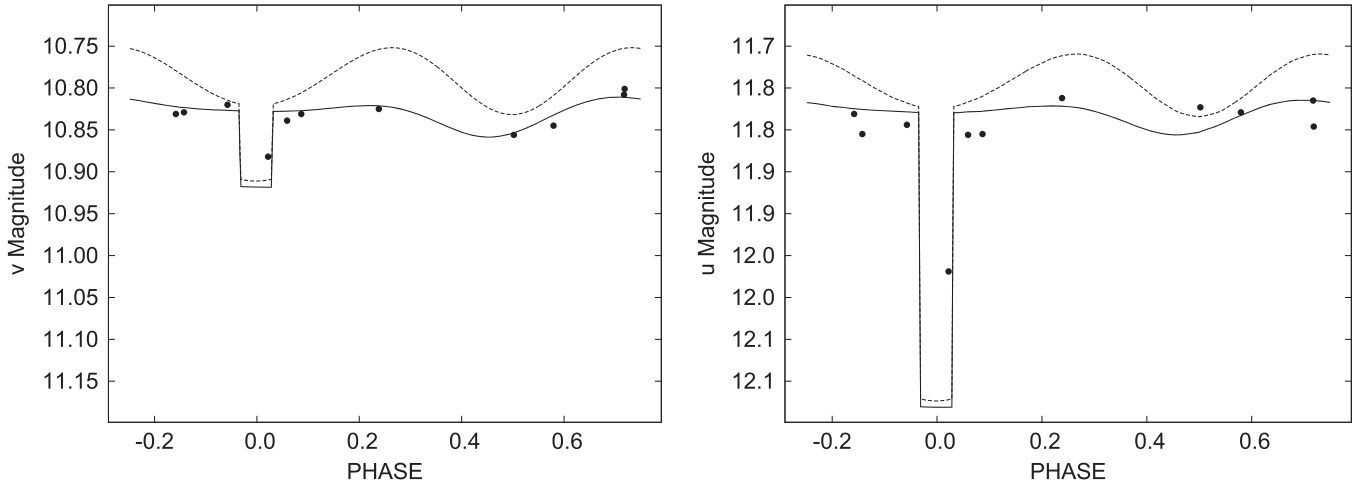

Figure 12. Same as Figure 11, but for the Rucinski (1983) *v* and *u* curves. Note the strong depth increase toward short wavelengths for eclipse of the very hot white dwarf.

11

Table 8
V471 Tau Multi-data-type Solutions

Parameter	All Data Excluding *MOST*	Times Only	*MOST* Light Curve Only	All Data Excluding *MOST* with Fixed Radii from *MOST*	All Data
a ($R_\odot$)	3.3827 ± 0.0024	...	3.3827	3.3628 ± 0.0024	3.3608 ± 0.0012
V_γ (km s^{-1})	36.91 ± 0.13	...	...	36.91 ± 0.13	36.88 ± 0.11
i (deg)	78.796 ± 0.059	...	78.796	78.809 ± 0.055	78.755 ± 0.030
T_1 (K)	34500	...	34500	34500	34500
T_2 (K)	5019 ± 8	...	5019	5084 ± 8	5066 ± 4
Ω_1	338.1 ± 3.1	...	315.50 ± 0.86	315.50	319.1 ± 1.4
Ω_2	5.0931 ± 0.0068	...	5.0691 ± 0.0018	5.0691	5.0646 ± 0.0033
M_2/M_1	1.1386 ± 0.0025	...	1.1386	1.1332 ± 0.0026	1.1360 ± 0.0016
T_0 (HJED $-$ 2445821.0)	0.898269 ± 0.000036	0.898293 ± 0.000043	0.898963 ± 0.000038	0.898270 ± 0.000036	0.898291 ± 0.000030
P_0[a] (days)	$0.5211833840(32)$	$0.5211833822(39)$	0.5211833840	$0.5211833844(32)$	$0.5211833875(27)$
dP/dt	$(+0.295 \pm 0.012) \times 10^{-10}$	$(+0.297 \pm 0.015) \times 10^{-10}$	$+0.295 \times 10^{-10}$	$(+0.293 \pm 0.013) \times 10^{-10}$	$+0.286 \pm 0.011 \times 10^{-10}$
$L_1/(L_1 + L_2)_u$	0.2533 ± 0.0014	...	...	0.2511 ± 0.0014	0.2531 ± 0.0011
$L_1/(L_1 + L_2)_v$	0.07699 ± 0.00046	...	...	0.07868 ± 0.00046	0.07876 ± 0.00032
$L_1/(L_1 + L_2)_b$	0.03159 ± 0.00025	...	...	0.03316 ± 0.00026	0.03296 ± 0.00014
$L_1/(L_1 + L_2)_y$	0.01775 ± 0.00016	...	...	0.01883 ± 0.00016	0.018660 ± 0.000084
$L_1/(L_1 + L_2)_B$	0.05239 ± 0.00036	...	...	0.05435 ± 0.00036	0.05419 ± 0.00022
$L_1/(L_1 + L_2)_V$	0.01829 ± 0.00016	...	...	0.01935 ± 0.00017	0.019193 ± 0.000085
$L_1/(L_1 + L_2)_{RC}$	0.01041 ± 0.00011	...	...	0.01117 ± 0.00011	0.011035 ± 0.000054
$L_1/(L_1 + L_2)_{IC}$	0.006190 ± 0.000070	...	...	0.006700 ± 0.000073	0.006604 ± 0.000035
$L_1/(L_1 + L_2)_{MOST}$	...	...	0.02133 ± 0.00011	...	0.019859 ± 0.000090
a_{3b} ($R_\odot$)	2588 ± 11	2576 ± 13	2588	2576 ± 11	2582 ± 10
P_{3b} (days)	10932 ± 71	10960 ± 83	10932	10949 ± 72	10996 ± 60
i_{3b} (deg)	90	90	90	90	90
e_{3b}	0.418 ± 0.022	0.435 ± 0.026	0.418	0.417 ± 0.022	0.392 ± 0.018
ω_{3b} (rad)	1.194 ± 0.053	1.180 ± 0.060	1.194	1.187 ± 0.053	1.369 ± 0.047
T_{03b} (HJED)	2441781 ± 53	2441784 ± 61	2441781	2441773 ± 53	2441910 ± 48
$f(m_3)$ ($M_\odot$)	1.14×10^{-5}	...	1.14×10^{-5}	1.15×10^{-5}	1.17×10^{-5}
a vs. a_{3b} correlation	0.128	...	...	0.127	-0.040

Note.

[a] Printed to two significant figures in its standard error, with the number in parentheses being the standard error in the last printed digits.

Table 9
V471 Tau Auxiliary Parameters and Absolute Dimensions

Parameter	Star 1	Star 2
	All Data Solution Excluding *MOST*	
r(pole)	0.002978 ± 0.000027	0.27195 ± 0.00053
r(point)	0.002978 ± 0.000027	0.28857 ± 0.00071
r(side)	0.002978 ± 0.000027	0.27731 ± 0.00057
r(back)	0.002978 ± 0.000027	0.28449 ± 0.00065
$<r>$[a]	0.002978 ± 0.000027	0.27738 ± 0.00047
K (km s^{-1})	171.5	150.6
M ($M_\odot$)	0.8939 ± 0.0018	1.0177 ± 0.0021
R ($R_\odot$)	0.010040 ± 0.000092	0.9383 ± 0.0019
$\log g$ (cm s^{-2})	8.3860 ± 0.0080	4.5011 ± 0.0017
$M_{\rm bol}$	6.982 ± 0.021	5.5007 ± 0.0091
	All Data Solution with Fixed Radii from *MOST*	
r(pole)	0.003052 ± 0.000026	0.27109 ± 0.00051
r(point)	0.003052 ± 0.000026	0.28761 ± 0.00069
r(side)	0.003052 ± 0.000026	0.27641 ± 0.00056
r(back)	0.003052 ± 0.000026	0.28357 ± 0.00063
$<r>$[a]	0.003052 ± 0.000028	0.27790 ± 0.00047
K (km s^{-1})	170.1	150.1
M ($M_\odot$)	0.8804 ± 0.0018	0.9977 ± 0.0020
R ($R_\odot$)	0.010697 ± 0.000096	0.9345 ± 0.0018
$\log g$ (cm s^{-2})	8.3243 ± 0.0078	4.4960 ± 0.0016
$M_{\rm bol}$	6.844 ± 0.021	5.4536 ± 0.0091
	All Data Solution	
r(pole)	0.003137 ± 0.000014	0.27240 ± 0.00028
r(point)	0.003137 ± 0.000014	0.28920 ± 0.00038
r(side)	0.003137 ± 0.000014	0.27780 ± 0.00031
r(back)	0.003137 ± 0.000014	0.28507 ± 0.00035
$<r>$[a]	0.003137 ± 0.000014	0.27883 ± 0.00025
K (km s^{-1})	170.2	149.8
M ($M_\odot$)	0.8778 ± 0.0011	0.9971 ± 0.0012
R ($R_\odot$)	0.010571 ± 0.000047	0.93709 ± 0.00093
$\log g$ (cm s^{-2})	8.3333 ± 0.0038	4.49331 ± 0.00087
$m_{\rm bol}$	6.870 ± 0.010	5.4630 ± 0.0051

Note.
[a] Brackets indicate equal-volume radii. Relative radius, r, is R/a.

in two ways—as part of the multi-data-type nonabsolute solutions and also in separate absolute solutions.

Table 8 has results from five input data-type combinations:

1. all data except the *MOST* light curve;
2. timings only;
3. the *MOST* light curve only;
4. all data except *MOST* but with the stellar radii fixed at the *MOST*-only solution values, thereby taking advantage of *MOST*'s high temporal density to resolve the fast partial eclipse jumps;
5. all data, including *MOST*.

Auxiliary parameters and absolute dimensions are given in Table 9. Although our derived masses are larger than those in OBBS (see Section 6), the red dwarf and white dwarf radii are virtually the same as theirs. Based on the 3b mass function in Table 8 (essentially independent of solution type), 3b masses for three orbit inclinations (i_{3b}) are given in Table 10. The 3b mass, M_3, exceeds the core hydrogen-burning threshold of

Table 10
Third-body Mass

i_{3b}	M_3 ($M_\odot$)
90°	0.03498 ± 0.00046
60°	0.04047 ± 0.00054
30°	0.07083 ± 0.00096

$0.07\ M_\odot$ only for i_{3b} below 30°, which makes the third body a likely brown dwarf candidate, in agreement with the conclusions of Guinan & Ribas (2001) and Ibanoglu et al. (2005). Selected observed and computed RV curves are compared in Figures 13–15. Figures 1–9 include computed light curves based on the Table 8 results.

5. TIMING RESIDUAL EXCURSIONS HISTORICALLY INTERPRETED AS A LIGHT-TIME EFFECT

Herczeg (1975) tentatively considered a 3b light-time interpretation of the timing residuals with a period around 5 yr—much shorter than recent estimates of 30+ yr. Existing data in 1975 covered only about 5 yr around the first observed maximum in the timing residual diagram, from about JD 2,440,500 to 2,442,300. Rather than turn upward, as expected for a 5 yr periodicity, the residual curve continued downward. Other early interpretations in terms of true period changes (Young & Lanning 1975; Tunca et al. 1979) mentioned implausibly large dP/dt values, perhaps due to misstated units. The idea of successive changes in the EB period, separated by intervals of constancy (Oliver & Rucinski 1978), was then about as well regarded as the light-time hypothesis.

A decade later, Beavers et al. (1986) reexamined the 3b hypothesis with timings that extended nearly to JD 2,446,100 and found a period of 24.6 yr, although the descending residuals had not yet turned upward. Skillman & Patterson (1988) argued against a 3b light-time interpretation on grounds that it does not explain all wiggles in the residual diagram and that residual variations similar to V471 Tau's appear in binaries that are thought not to have third-star companions. Bois et al. (1991) repeated the Beavers et al. analysis, with some procedural changes and the same data, finding again a P_{3b} of 24.6 yr and a slightly different light-time amplitude. With nearly another decade of timings in hand—seemingly most of a cycle—Ibanoglu et al. (1994) came up with a P_{3b} of—again—24.6 yr. Then from essentially a full cycle, Guinan & Ribas (2001) found a period of 30.5 yr—considerably longer than any before. The increase is likely due to near completion of the diagram's rising branch, which is less steep than had been estimated from substantially less than a cycle, thereby taking longer than expected to reach the peak. Next, Ibanoglu et al. (2005) published similar results from eclipse times that continued the trend to a longer period, with P_{3b} = 32.4 yr. Kaminski et al. (2007) and Hric et al. (2011) then found 3b periods of 33.7 and 33.2 yr, respectively, with other parameters roughly similar to those of Guinan & Ribas (2001) and Ibanoglu et al. (2005). Our all-data P_{3b} of 30.11 $\pm$ 0.16 yr (Table 8, column 6) is the same as the 30.5 $\pm$ 1.6 yr by Guinan & Ribas within the uncertainty, although $e_{3b} \approx 0.39$ and $\omega_{3b} \approx 1.37$ rad, both parameters being somewhat larger than found by Guinan & Ribas (respectively, 0.31 and 1.09 rad) from timings only and for a shorter timewise baseline.
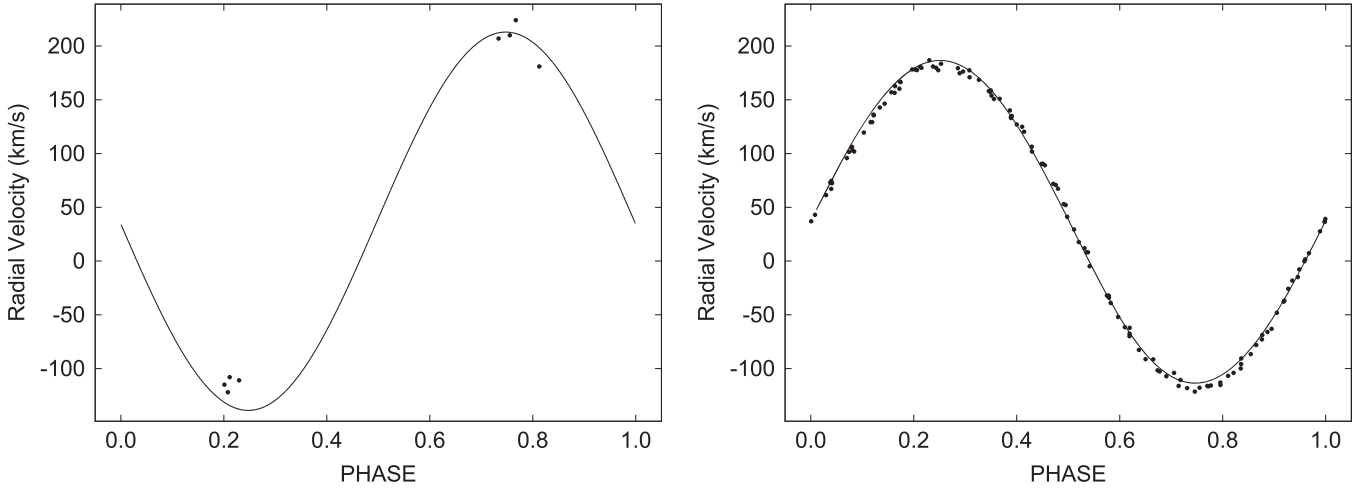
Figure 13. Left panel: white dwarf radial velocities from 1994 to 1995 by O'Brien et al. (2001) and fixed-radius solution (last column of Table 8) curve. Only the seven velocities in the interval HJED 2,449,643–2,449,651 are shown, with the phased curve computed for the cycle that starts near HJED 2,449,648.427. Right panel: KPNO red dwarf radial velocities (this paper) and computed curve for the cycle that starts near HJED 2,451,126.0.
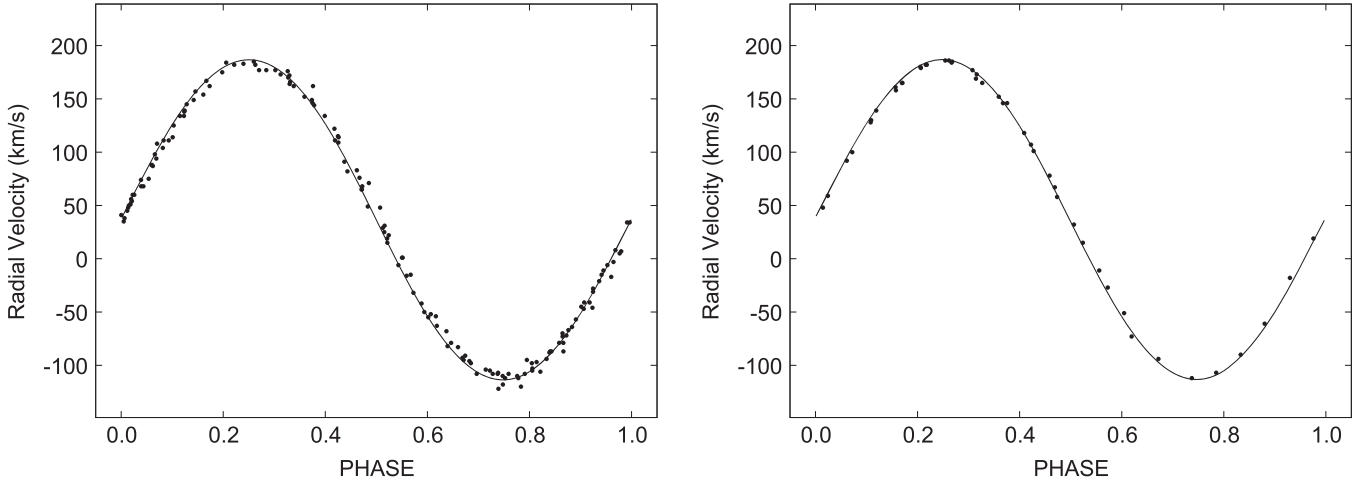

Figure 14. Left panel: red dwarf RVs by Bois et al. (1988) for velocities between HJED 2,443,185 and HJED 2,444,281 and curve for the fixed-radius solution for the cycle that starts near HJED 2,443,828.4. Right panel: same as the left panel, but for velocities between HJED 2,445,644 and HJED 2,445,648, with the computed curve for the cycle that starts near HJED 2,445,646.3.
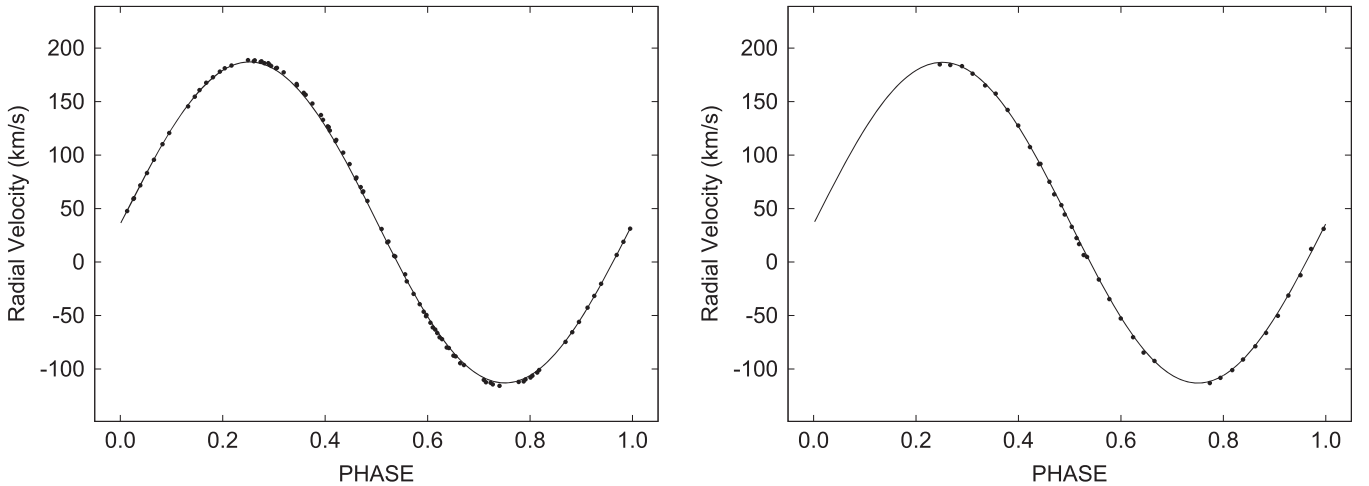
Figure 15. Left panel: red dwarf RVs (Hussain et al. 2006) and curve for the fixed-radius solution at the cycle that starts near HJED 2,452,603.0. Right panel: red RVs by Kaminski et al. (2007), with a computed curve for the cycle that starts near HJED 2,453,717.8.
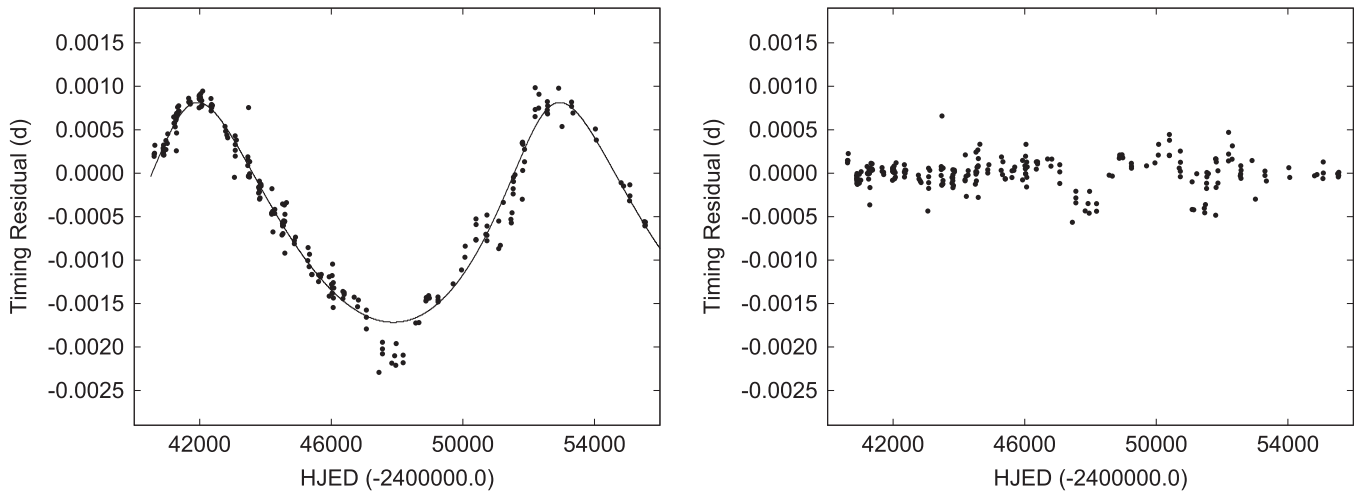
Figure 16. Residuals for the timing-only solution. The left panel shows residuals without a modeled 3b light-time effect. The solid curve shows the corresponding idealized behavior. The right panel is for the full ephemeris/light-time solution. Unexplained features of order 2000 days wide that have not attracted comment in the literature are centered on roughly JD 2,448,00 and JD 2,453,000.
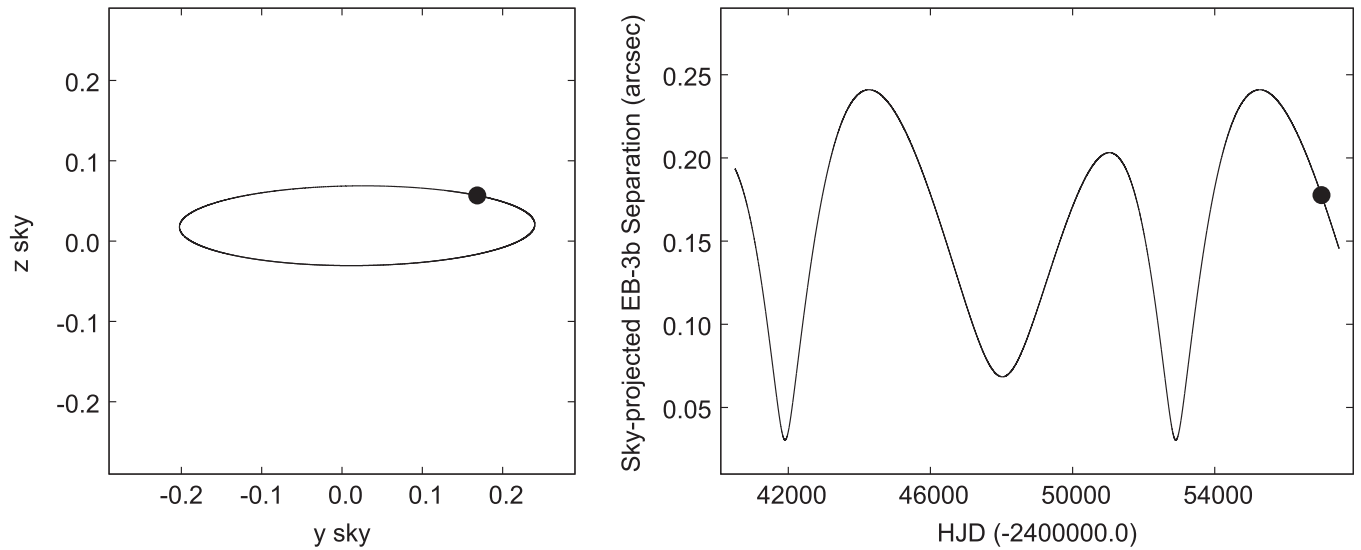
Figure 17. Computed 3b minus EB sky coordinates in arcseconds (left panel) and separation vs. time (right panel) for parameters of the all-data solution (column 3 of Table 8) and a 3b inclination of 78°. The dot indicates the position of the 3b on 2014 December 11 (the date of the AO observation by Hardy et al. 2015). Motion of the 3b dot in the left panel is counter-clockwise. The EB is at the origin of coordinates.

Although Kaminski et al. (2007) computed 3b parameters, they considered two explanations for the timing diagram that did not involve a third star—apsidal motion in a slightly eccentric orbit and actual orbital period changes for the EB. In any case, the overall picture has been one of increasing period estimates for the light-time effect, although the situation may now have stabilized, as the long-awaited second historical downturn in the timing residuals has finally occurred, as shown by Figure 16. Another 12 yr of timings have arrived since the Guinan & Ribas paper and unification solutions now can include whole light curves and RVs, with proper weighting. Our various solutions that properly separate true period change from light-time effect find quite small dP/dt values of order $+3 \times 10^{-11}$, typically differing from zero by about 20σ. Timing residual diagrams for the all-data solutions of Table 8 look essentially the same as Figure 16, so they are not shown.

More can now be said about the reality of the 3b component with the help of another decade and a half of timing observations. Residuals from a linear ephemeris have the form expected for a 3b light-time effect, as shown by Figure 16. Actually, the form was already right in Figure 2 of Guinan & Ribas, but the additional timings make the agreement with expectation significantly clearer. More than one cycle is now in hand, and the data points are repeating! There are two disturbances, but that is a familiar experience with EB timing diagrams, which only rarely repeat with all "desired" accuracy. Mainly the observed and computed timing residual curves agree. However, some EB timing diagrams have repeated for part of a second cycle, but not after that, so a stronger timing-based decision on V471 Tau's light-time effect may have to await several more decades.

The outer orbit's orientation within its own plane, specified by argument of periastron ω_{3b}, affects eclipse times via the light-time effect and affects results from the other two data types to some extent. The outer orbit is too large to show significant rotation over the 40+ yr of observation, so one cannot expect to measure $d\omega_{3b}/dt$.
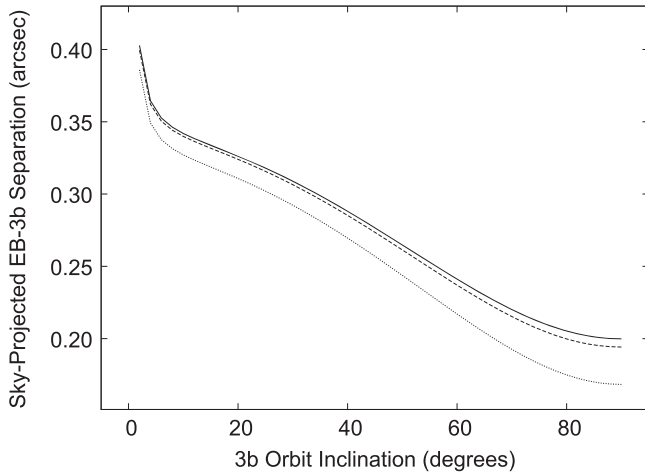
15

Figure 18. Computed EB-3b sky separation vs. 3b orbit inclination on 2014 December 11 (the reference date for Figure 3 of Hardy et al. 2015). The solid, dashed, and dotted lines are for parameters of the timing-only (column 3 of Table 8), no-*MOST* (column 2 of Table 8), and all-data (column 6 of Table 8) solutions, respectively.

6. THE RED DWARF'S MASS

The all-data M_2 of Table 9 that taps into virtually all existing and relevant V471 Tau mass information has $M_2 = 0.9971 \pm 0.0012\,M_\odot$. How can a K2 V star be as massive as the Sun? Although the envelope would likely be chemically contaminated by passage through a giant star envelope, a normal view of common envelope evolution would see the red dwarf as sufficiently close to chemical uniformity to be a well-adjusted main-sequence star. Given the K2 spectral type and radius within main-sequence limits, the red dwarf should have the mass of a K2 main-sequence star, around 0.70–$0.80\,M_\odot$. Section 5 of OBBS thoroughly examined this K2 V mass issue in the context of their $M_2 = 0.93 \pm 0.07\,M_\odot$ result, finding the star overmassive for the main sequence, and now our solutions produce the same outcome with a smaller formal uncertainty. The apparent discrepancy between observational and expected M_2 requires serious investigation, as it bears upon all V471 Tau evolutionary contributions and on the understanding of common envelope evolution. The M_2 determined in OBBS has been adopted for various applications (e.g., Guinan & Ribas 2001; Chatzopoulos et al. 2012; Parsons et al. 2012; Zorotovic & Schreiber 2013; Hardy et al. 2015), although one should remember that it is based on the only V471 Tau white dwarf RV curve ever published (also true of our M_2 result) and on one of only two red dwarf RV curves of the system in print at the time. Note also that the OBBS M_2's 1σ uncertainty of $0.07\,M_\odot$ allows a rather wide range of actual values, yet their M_2 is sometimes adopted without mention of that fact.

6.1. Investigation of the Apparent Red Dwarf Mass Anomaly

OBBS devoted two pages to discussion of measurement difficulties of their white dwarf RVs. The only useful white dwarf spectral line in their *Hubble Space Telescope* spectra was Lyα, which is *very* wide (about 40 Å), thus undermining its usefulness as a sharp RV marker. OBBS mention that the pre- and post-COSTAR systemic RVs (V_γ), determined independently of the red star RVs, differ by 60 km s^{-1}. They also write, "we feel that the absolute velocity zero point for Lyα is

Table 11
V471 Tau Individual Radial Velocity Solutions

Parameter	Young (1976)	Bois et al. (1988)	Table 1	Hussain et al. (2006)	Kaminski et al. (2007)
a ($R_\odot$)	3.31 ± 0.12	3.263 ± 0.048	3.320 ± 0.043	3.384 ± 0.057	3.317 ± 0.045
V_γ (km s^{-1})	38.4 ± 1.4	37.03 ± 0.36	35.54 ± 0.36	37.58 ± 0.20	35.94 ± 0.25
M_2/M_1	1.150 ± 0.081	1.101 ± 0.031	1.109 ± 0.028	1.114 ± 0.036	1.089 ± 0.029
K_1 (km s^{-1})	168.6	162.8	166.2	169.7	164.6
M_1 ($M_\odot$)	0.83	0.82	0.86	0.91	0.86
R_1 ($R_\odot$)	0.0104	0.0.0103	0.0104	0.0106	0.0104
K_2 (km s^{-1})	146.6	147.8	149.9	152.4	151.2
M_2 ($M_\odot$)	0.96	0.90	0.95	1.01	0.94
R_2 ($R_\odot$)	0.93	0.88	0.91	0.93	0.89

Note. Solutions are for the O'Brien et al. (2001) white dwarf radial velocities reduced by 10 km s^{-1} (see text for explanation), combined with each of the red dwarf velocity sets. There is no 3b light-time effect in the tabulated solutions. Separate solutions with a light-time effect gave very nearly the same results. Standard errors do not include uncertainties of parameters held fixed. RV semiamplitudes (K_1, K_2) are provided for readers who prefer to solve radial velocities in terms of semiamplitudes instead of direct astrophysical parameters.

untrustworthy because of the steep sensitivity function." Here the "steep sensitivity function" refers to the detector response being a steep function of wavelength across the wide Lyα line, thereby rendering the recorded line profile asymmetric and introducing a false wavelength (and velocity) shift. Presumably such a shift would be statistically the same for all of their RV measures. If so, it might not much affect the RV amplitude. However, line width consequences for RV amplitude are possible, although that issue was not included in the OBBS discussion.

6.1.1. Some Possibilities

Five ideas to account for the discrepancy between the OBBS mass results and ours were then checked computationally. All seemed unlikely to account for a significant part of the M_2 difference prior to the actual testing, but *something* must cause the anomaly, so the tests were made. Parameters that are essentially photometric were fixed at the all-data values of Table 8. The tests were:

1. allowing for a slight orbital eccentricity by solving with parameters e and ω adjusted;
2. searching for a local minimum in the parameter space of our solutions that might be deeper than that initially found;
3. checking on the effect of correlations between the "untrustworthy" V_γ of the white dwarf RVs and parameters a and M_2/M_1;
4. comparing RV-only solutions done with and without a 3b light-time effect (OBBS did not include a light-time effect);
5. examining results of our five RV-only solutions to see whether the red dwarf mass based on the Bois et al. (1988) data (the only red dwarf RVs used by OBBS) is typical of those from the other four sets.
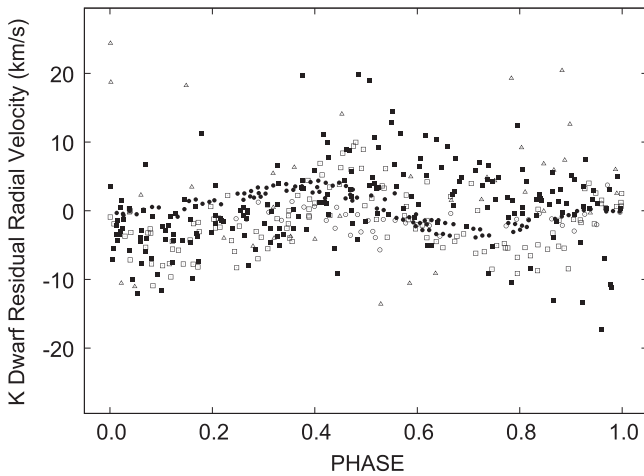
16

Figure 19. Red dwarf RV residuals for the all-data solution (column 6 of Table 8). Essential overlap of residuals for the five curves, even with relatively large scatter of the two older sets, shows essential agreement in amplitude among the curves, although there are small amplitude differences and subtle shape differences. Open triangles: Young (1976); filled squares: Bois et al. (1988); open squares: this paper (Table 1); filled circles: Hussain et al. (2006); open circles: Kaminski et al. (2007). The Young (1976) and Bois et al. (1988) data have low weights and influence the overall results only slightly. The Hussain et al. (2006) and Kaminski et al. (2007) velocities have highest weights.

Items 1–4 indeed turned out to be of little or no importance with regard to derived masses. Specifics are omitted in the interest of brevity. Item 5 led to some understanding, as the Bois et al. (1988) observations gave the lowest masses of the five red dwarf RV curves, as seen in Table 11.

Because the computed masses depend on the cube of the RV amplitude via Kepler's third law, small amplitude disagreements can have substantial consequences. This is clearly an RV problem, as light curves and timings of a well-detached EB carry almost no mass information. Therefore, separate RV-only solutions were carried out for the five red dwarf RV data sets, each solved together with the one white dwarf data set. Results are in Table 11. The purpose was to see whether the widely adopted M_2 result of OBBS is specifically characteristic of the (only) red dwarf RVs (Bois et al. 1988) entered into the OBBS analysis. Rather than apply a binary star model, OBBS simply fitted a sine curve to their white dwarf velocities to obtain two parameters, an amplitude and a (subsequently discarded) V_γ. Because our binary model analysis requires observations with a meaningful zero point, while OBBS reject any such zero point in their RV1s as "untrustworthy" (and did not mention a resulting V_γ), a preliminary exercise here was to fit the white dwarf RVs in the same way as stated by OBBS. Our thus-fitted sine curve led to an M_2 value close to that by OBBS when matched with an amplitude from the Bois et al. (1988) red star RVs,[14] also found from a fitted sine wave. V_γ for the white dwarf differed by 10 km s^{-1} from that of the all-data solution in Table 8. Accordingly, 10 km s^{-1} was subtracted from each white dwarf velocity entered into our five RV-only solutions (one for each published red dwarf velocity curve) so as to allow essential consistency between star 1 and star 2 RVs (our binary star analyses find one V_γ that serves for stars 1 and 2). Resulting mass differences among RV data sets in the test

---

[14] A precise match cannot be expected since the OBBS data weighting may have differed from ours.

solutions are very much larger than the corresponding σ's of the masses in Table 9, which are *internal* uncertainties that do not account for systematic data set errors, most notably in RV amplitudes. Apparently such systematic errors, although not striking, are significant in most or perhaps all of the RV curves (see Figure 19). The M_2 values in Table 11 range from 0.90 $M_\odot$ (Bois et al. RVs) to 1.01 $M_\odot$ (Hussain et al. RVs). With two of the more precise red dwarf RVs, M_2 is 0.04 $M_\odot$ and 0.11 $M_\odot$ higher than with the Bois et al. (1988) RVs, thus accounting, respectively, for about half (Kaminski et al.) or slightly more than all (Hussain et al.) of the discrepancy between our M_2 and that of OBBS. Since the OBBS M_2 utilized only the Bois et al. RVs for the red dwarf (those giving the lowest M_2 of the five data sources), while the largest M_2 is from the recent highly precise and accordingly highly weighted Hussain et al. data set, our high M_2 from the all-data solution is probably explained.

6.1.2. A Summary of the Investigation on Mass Results

A brief summary of mass findings may be useful. First, a preliminary exercise showed that the OBBS masses are essentially recovered when their procedure is followed and the Bois et al. RVs are adopted. Then solution experiments dismissed items 1–4 (Section 6.1.1) as unimportant. Next, the data set dependence was isolated via RV-only solutions for the five red dwarf (plus one white dwarf) RV data sets. One can examine the mass entries of Table 11 to see how the derived red dwarf and white dwarf masses change from data set to data set. The RVs from Bois et al. (1988) give the lowest masses. We find that the red dwarf mass of 0.93 $M_\odot$ derived by OBBS, and properly called high for a K2 V star, actually comes out somewhat higher (now $M_2 \approx 1.00 \, M_\odot$) if all of the now-existing RV data are utilized, properly weighted. A revised evolutionary explanation seems needed unless new RVs of the white dwarf can give an observational way out. Such an explanation cannot be developed now since, even if the K2 star did spiral through a giant star envelope, the specifics of the encounter (giant star's chemical profile, etc.) are uncertain, as is subsequent radial redistribution by convection and advection within the resulting (now K2) star. A very simple assumption, that the K2 star became uniformly enriched in metals, goes in the right sense to account for the mass anomaly, as the red star would then lie to the right of the solar-composition main sequence, explaining its late spectral type in terms of composition rather than mass. However, uniform enrichment seems unlikely. In the alternative (observational) fix, the much-cited mass results may need revision based on new white dwarf RVs, although that will be difficult owing to the white dwarf's faintness.

7. PHOTOMETRIC–SPECTROSCOPIC DISTANCE

EB light curves allow measurement of relative radii, $R_{1,2}/a$, while RVs set the geometric scale via the orbital semimajor axis parameter, a. These steps are combined in simultaneous light/RV solutions. With a full physical model that specifies local radiative behavior at all points on both stars, observable bandpass flux at given aspect and distance can be computed in standard physical units and compared with observed fluxes in those units. Numerical inversion of this parameters-to-flux problem can yield distance in parsecs if distance is one of the parameters. Specifics and examples of the process are in

Table 12
BD −3°5358 Magnitudes

HJD (−2,450,000.0)	HJED (−2,450,000.0)	Standard Magnitude
5812.6603	5812.6611	$B = 11.036 \pm 0.002$
5833.6032	5833.6040	$B = 11.032 \pm 0.002$
6199.7300	6199.7308	$B = 11.054 \pm 0.008$
6235.6286	6235.6294	$B = 10.992 \pm 0.006$
5812.6600	5812.6608	$V = 10.355 \pm 0.001$
6199.7301	6199.7309	$V = 10.370 \pm 0.006$
6235.6286	6235.6293	$V = 10.396 \pm 0.005$
6199.7344	6199.7352	$g' = 10.665 \pm 0.005$
6235.6330	6235.6338	$g' = 10.664 \pm 0.004$
5833.6041	5833.6049	$r' = 10.322 \pm 0.001$
6199.7305	6199.7312	$r' = 10.160 \pm 0.005$
6235.6289	6235.6297	$r' = 10.192 \pm 0.004$
5812.6627	5812.6634	$i' = 10.008 \pm 0.002$
5833.6054	5833.6062	$i' = 10.127 \pm 0.002$
6199.7308	6199.7316	$i' = 10.036 \pm 0.010$
6235.6293	6235.6301	$i' = 10.025 \pm 0.008$

Note. Bands g', r', and i' are Sloan Digital Sky Survey systems. Transformations from Sloan to R_C and I_C have been developed by U. Munari (A.A. Henden 2015, private communication). The transformations are $R_C = r' - 0.17122 - 0.07747(V - i') - 0.02902(V - i')^2$, and $I_C = i' - 0.37313 - 0.11431(V - i') + 0.01066(V - i')^2$.

Wilson (2008), with further examples in Wilson & van Hamme (2009), Vaccaro et al. (2010), and Wilson & Raichur (2011). A separate distance estimation step with spherical star assumptions and other simplifications is no longer needed.

The best current V471 Tau distance estimate is likely that by de Bruijne et al. (2001) from secular parallax (48.64 ± 0.78 pc), while EB photometric–spectroscopic distance and trigonometric parallax distance have larger uncertainties for V471 Tau but give welcome checks. Interstellar extinction can be a major cause of photometric–spectroscopic distance inaccuracy but probably is negligible for Hyades objects in optical and infrared bands. Only one spectroscopic temperature is needed for favorable EBs where eclipse depths for both stars establish a relation between the two temperatures. However, eclipses of V471 Tau's red star by its white dwarf companion are not realistically observable at present, so the distance cannot be estimated in the usual way from light and RV curves without prior temperature knowledge for both stars. Good spectroscopic temperatures are known for both V471 Tau components, so a photometric–spectroscopic distance can be computed in an absolute solution, as only one distance will be compatible with the observed absolute fluxes and other system parameters. Those other parameters are already known from the nonabsolute solutions of Table 8 and can be taken from the table and applied to the (absolute) distance solution. Alternatively (not done in this paper), all adjustable parameters can be determined in an (absolute) distance solution.

The *MOST* data were not in the distance solutions because their absolute photometric calibration is not well known. V471 Tau's distance was found from the Rucinski light curves, as they are on the standard *uvby* system and the comparison star magnitudes are known. Its distance was also found from the KPNO photometry of Table 2 after conversion of the differential instrumental magnitudes, Δm_B and Δm_V, to standard B and V magnitudes. The transformations are based on our 1998 KPNO instrumental magnitudes of BD +16°515

and BD −3°5358, on BD +16°515's standard B and V means of Table 3, and on standard B and V measures of BD −3°5358 made from 2011 September 8 to 2012 November 11 and provided in Table 12. BD +16°515 and BD −3°5358 have an acceptable color difference and thereby give satisfactory transformations as BD +16°515 is redder than BD −3°5358 by about 0.53 mag in $B - V$. The tabulated Δm_B and Δm_V values were converted to B and V, respectively, via

$$B = B_{\mathrm{comp}} + \Delta m_B + 0.2695(\Delta m_B - \Delta m_V) \tag{1}$$

and

$$V = V_{\mathrm{comp}} + \Delta m_V - 0.1090(\Delta m_B - \Delta m_V), \tag{2}$$

where B_{comp} and V_{comp} are from the means in Table 3. Required flux calibrations for u, v, b, y, B, and V are from Table 1 of Wilson et al. (2010). Individual single-band curves were solved for distance with stepped input of surface temperature for both the white dwarf and red dwarf, with results in Table 13. The reasons for stepping the temperatures are (a) to give a realistic impression of how strongly distance results depend on temperature input, and (b) to allow interpolation if temperature estimates improve (although they already seem rather consistent among authors). Distances for the six T_1, T_2 combinations and six photometric bands sprinkle from about 41.4 to 54.6 pc, which is a larger range than for normal EBs that have two observable eclipses per cycle. We are reminded that V471 Tau is a difficult object.

Distance accuracy for V471 Tau is affected to some extent by uncertainty in spottedness (spot latitudes, longitudes, sizes, temperatures, growth and decay, and drift motions), but bolometric luminosity (and, to first order, bandpass luminosity) should not be changed very much since convective energy flow that is blocked by the magnetic fields of spots must come out elsewhere. The distances of Table 13 and others in the literature are remarkably close in aggregate to Hyades distance estimates, considering that V471 Tau does not project upon the cluster core, being approximately $10°$ (≈ 8 pc) from the center, which is well outside the tidal radius (≈ 3 pc) and core radius. At that projected separation, it would not have been surprising if V471 Tau were a similar linear distance nearer or farther than the Hyades center. However, the V471 Tau distances, taken as a whole, seem reasonably well determined, so the close match may just be a coincidence. Anyway, the system's location within the Hyades seems well established.

8. OTHER PERIODIC LIGHT AND VELOCITY CHANGES

Ibanoglu et al. (1994, 2005) mention a periodic fluctuation in the timing residuals of about 5 or 5.5 yr, possibly modulated by a concurrent periodic change in average brightness. Kaminski et al. (2007) briefly discuss a 10 yr cycle and suggest that it may be due to an activity cycle on the red dwarf surface. A Lomb–Scargle (Lomb 1976; Scargle 1982) period search in our timing-only residuals found three (all of low power) peaks near 13, 9, and 5 yr. Sinusoids of the form

$$\mathcal{A} + \mathcal{B} \sin\left[(2\pi/P)(t - t_0)\right] \tag{3}$$

were fitted to the residuals from the timing solution of column 3 in Table 8. Derived parameters for Equation (3) are in Table 14, and corresponding curves are in Figures 20–22. Possible mechanisms could include the magnetic phenomenon proposed by Applegate (1992).

Table 13
Absolute Solutions and Distance

T_1 (K)	T_2 (K)	u	v	b	y	B	V
34500	5000	49.73 ± 0.45	53.50 ± 0.41	54.45 ± 0.42	54.59 ± 0.66	52.14 ± 0.15	52.13 ± 0.28
34500	4900	45.57 ± 0.43	49.27 ± 0.37	50.96 ± 0.39	51.46 ± 0.62	48.43 ± 0.13	49.05 ± 0.25
34500	4800	41.79 ± 0.42	45.22 ± 0.34	47.53 ± 0.36	48.36 ± 0.57	44.84 ± 0.12	45.99 ± 0.22
33500	5000	49.42 ± 0.45	53.41 ± 0.40	54.41 ± 0.42	54.57 ± 0.66	52.08 ± 0.15	52.11 ± 0.28
33500	4900	45.23 ± 0.42	49.17 ± 0.37	50.92 ± 0.38	51.44 ± 0.61	48.37 ± 0.13	49.03 ± 0.25
33500	4800	41.42 ± 0.41	45.11 ± 0.34	47.48 ± 0.35	48.34 ± 0.57	44.77 ± 0.12	45.97 ± 0.22

Note. Distance in parsecs from single-band Direct Distance Estimation (DDE) solutions is given for stepped input of two white dwarf and three red dwarf temperatures, so as to allow interpolation if knowledge of the star temperatures improves. The standard errors are from individual solutions that also adjusted the full set of parameters from our all-data solution. Starting values of other parameters are from the all-data nonabsolute solution of Table 8.

Table 14
Timing Residual Fitted Sinusoids

$\mathcal{A}$ (days)	$\mathcal{B}$ (days)	t_0 (HJED)	P (yr)	σ (days)
$(0.02 \pm 0.12) \times 10^{-4}$	$(0.81 \pm 0.17) \times 10^{-4}$	2443797 ± 158	13.01 ± 0.43	0.0001669
$(0.02 \pm 0.11) \times 10^{-4}$	$(0.70 \pm 0.16) \times 10^{-4}$	2443989 ± 77	5.486 ± 0.093	0.0001685
$(0.10 \pm 0.12) \times 10^{-4}$	$(0.66 \pm 0.17) \times 10^{-4}$	2445573 ± 125	9.00 ± 0.26	0.0001694
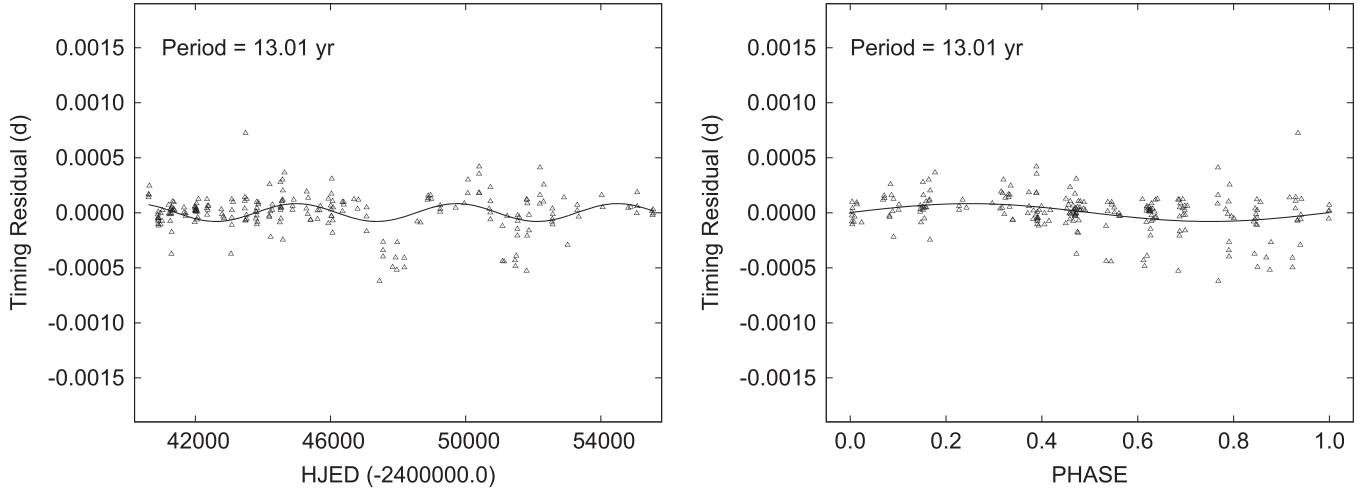
Figure 20. Residuals for the timing-only solution with a fitted sinusoid of period 13.01 yr (left panel) and the corresponding phased curve (right panel).
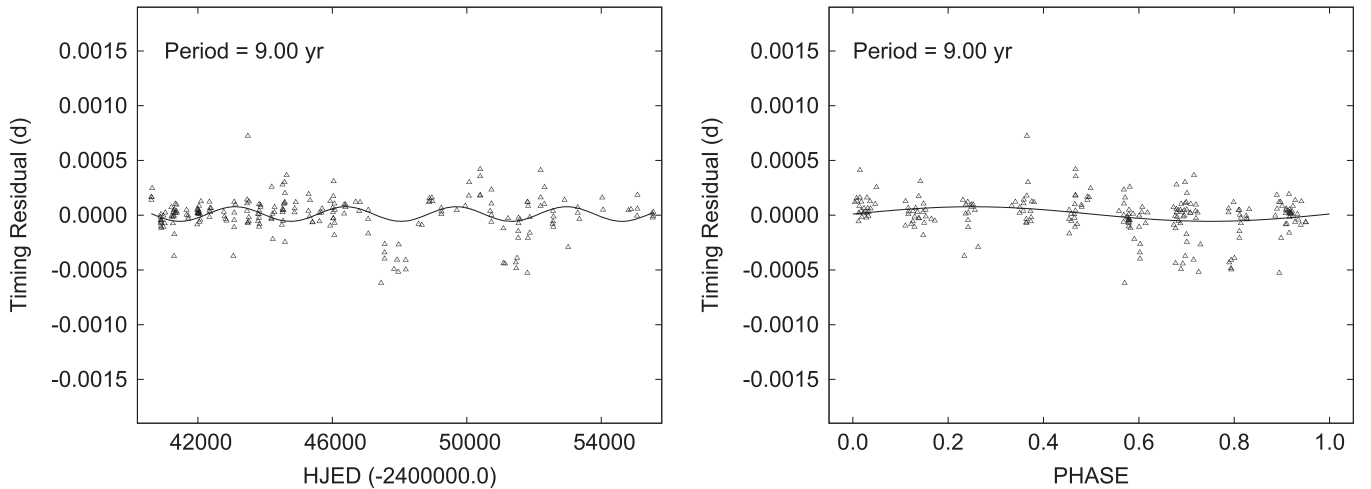
Figure 21. Same as Figure 20, but for a period of 9.00 yr.
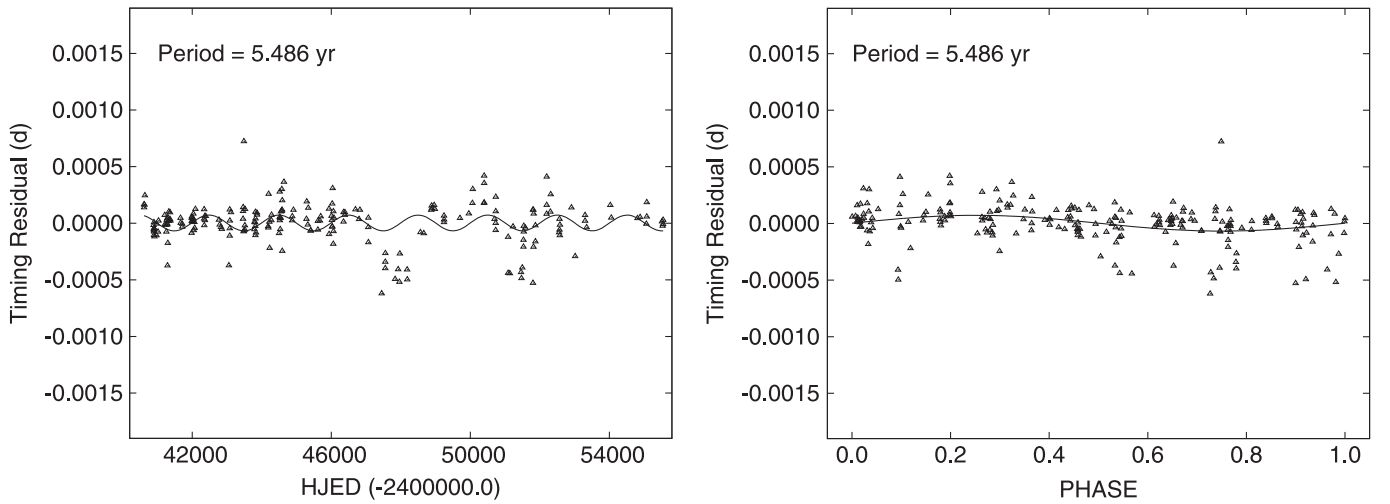
Figure 22. Same as Figure 20, but for a period of 5.486 yr.
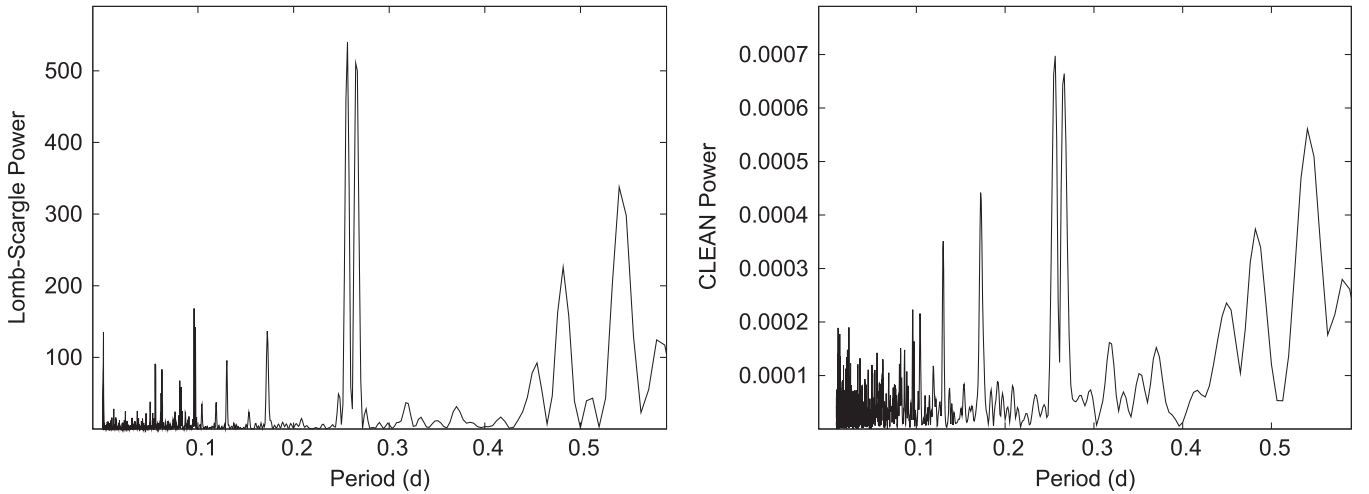
Figure 23. *MOST* residual magnitude Lomb–Scargle (left) and CLEAN (right) periodograms.

A close look at the residuals in many of the photometric bands and the red dwarf velocity curves reveals a much shorter periodicity, $\approx$0.26 days, a value nearly indistinguishable from half the orbital period. This variation is clearly visible in the residual velocity graph in Figure 1 of Hussain et al. (2006), who attribute it to perturbations by spots. Many of the light curves show the phenomenon, although our modeled spots should have removed spot effects from the residuals, at least in first approximation. Assuming synchronization with the orbit period, the fundamental of a variation that arises from a variable tide in a slightly eccentric orbit would be very difficult to detect in competition with ordinary proximity effects (reflection and ellipsoidal variation), but its harmonics may be easier to find. Accordingly, searches were made via the Lomb–Scargle and CLEAN (Roberts et al. 1987) algorithms for signatures of harmonics near 2, 3, and 4 times the orbital frequency. Because of its high density of points and absence of major gaps, the *MOST* residual curve is the one best suited to a search for such frequencies. The Lomb–Scargle and CLEAN periodograms of the *MOST* residuals are in Figure 23. Their more prominent peaks coincide, although not with the same order of relative height. Results of least-squares fits of Equation (3) to the *MOST*-only residuals (column 4 of

Table 8), starting with the periods of the six highest periodogram peaks, are in Table 15 and Figures 24–27. Similar fits for periods close to 0.26 days were made for the KPNO residual light curves and the red dwarf RV residuals from the all-data solution in the last column of Table 8, with parameters in Table 15 and waveforms in Figures 28–34. The overall outcome is that there *are* close matches between harmonics of the orbit period and the identified periodicities, but the latter's very small σ's indicate that the matches are not formally valid. Continued light-curve monitoring could further quantify these correspondences.

As a causal candidate for the 0.26 day periodicity, one might consider the first harmonic of a tidal oscillation, whose fundamental frequency would be $1/P_{\mathrm{orb}}$ s^{-1}. The slight orbital eccentricity needed to drive the tide may have already been found by Kaminski et al. (2007), whose Table 4 gives $e = 0.0121 \pm 0.0006$ from eclipse timings, and whose Table 6 gives 0.012 ± 0.003 from the red dwarf RVs. While caution is the watchword for acceptance of such small eccentricities from RVs (Lucy & Sweeney 1971, 1973), these measures from two unrelated data types are formally 20σ and 4σ results! To explore the possibility of a nonzero eccentricity, both the Kaminski et al. and Hussain et al. red dwarf RVs were solved, allowing eccentricity, e, and argument of periastron, ω, to

Table 15
Magnitude and Velocity Residual Fitted Sinusoids

Band	$\mathcal{A}$ (mag)	$\mathcal{B}$ (mag)	t_0 (HJED)	P (days)	$P_{harmonic}$ (days)	σ (mag)
			Periodicities from Light-curve Residuals			
MOST	$(-0.12 \pm 0.37) \times 10^{-4}$	0.001913 ± 0.000052	2453713.4518 ± 0.0011	0.256040 ± 0.000097	0.26059	0.002849
MOST	$(-0.17 \pm 0.37) \times 10^{-4}$	0.001878 ± 0.000052	2453713.3206 ± 0.0012	0.26568 ± 0.00011	0.26059	0.002853
MOST	$(-0.14 \pm 0.40) \times 10^{-4}$	0.000954 ± 0.000056	2453713.3726 ± 0.0016	0.172546 ± 0.000095	0.17373	0.003079
MOST	$(-0.09 \pm 0.40) \times 10^{-4}$	0.000818 ± 0.000058	2453713.4947 ± 0.0014	0.130151 ± 0.000062	0.13030	0.003100
B	$(+0.26 \pm 0.26) \times 10^{-3}$	0.00391 ± 0.00036	2451122.3797 ± 0.0040	0.26294 ± 0.00038	0.26059	0.0077
V	$(-0.019 \pm 0.25) \times 10^{-3}$	0.00176 ± 0.00038	2451122.3968 ± 0.0083	0.27644 ± 0.00081	0.26059	0.0072
R_C	$(-0.080 \pm 0.25) \times 10^{-3}$	0.00144 ± 0.00035	2451122.421 ± 0.011	0.2734 ± 0.0010	0.26059	0.0071
I_C	$(-0.21 \pm 0.26) \times 10^{-3}$	0.00267 ± 0.00038	2451122.6890 ± 0.0058	0.27675 ± 0.00055	0.26059	0.0065
			Periodicities from Red Dwarf Radial Velocity Residuals			
RV Set	$\mathcal{A}$ (km s^{-1})	$\mathcal{B}$ (km s^{-1})	t_0 (HJED)	P (days)	$P_{harmonic}$	σ (km s^{-1})
RV2 (Bois)	-0.08 ± 0.49	2.35 ± 0.67	2445646.188 ± 0.012	0.2546 ± 0.0025	0.2606	3.1421
RV2 (KPNO)	-2.00 ± 0.33	2.95 ± 0.47	2451121.7252 ± 0.0066	0.26029 ± 0.00053	0.2606	3.6878
RV2 (Hussain)	0.42 ± 0.16	1.69 ± 0.23	2452603.1660 ± 0.0057	0.2593 ± 0.0012	0.2606	1.5842
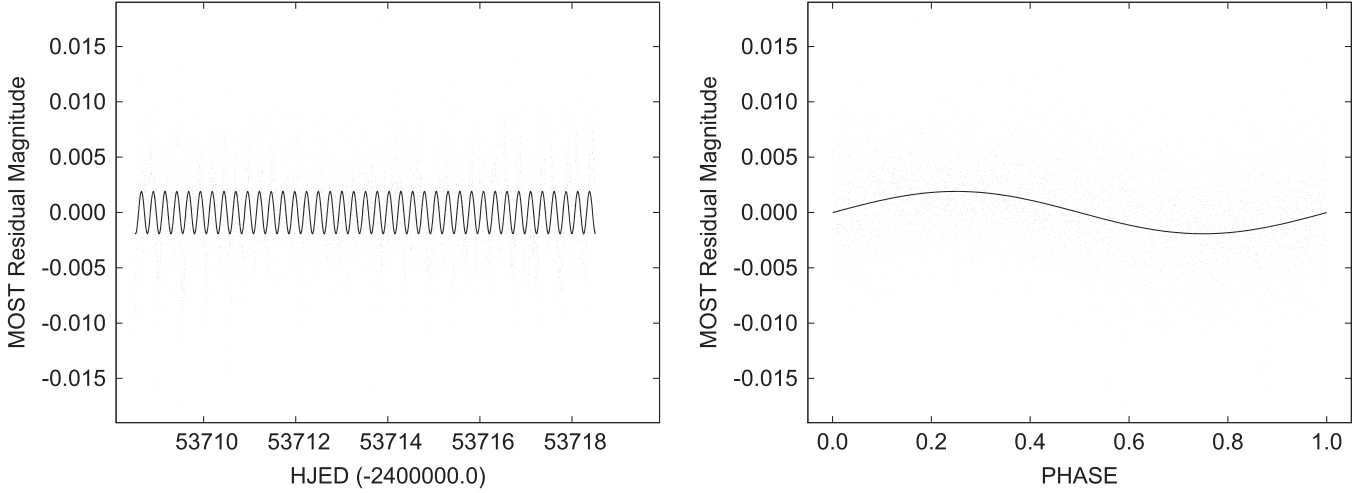
Figure 24. Residual magnitude and fitted sinusoid (left panel) for the *MOST* light curve for a detected 0.26568 day periodicity, nearly half the orbit period. The phased curve is in the right panel. Given the large quantity of points, the variation cannot be a statistical artifact. (This figure may not appear optimally in some browsers, resulting in missing data points).
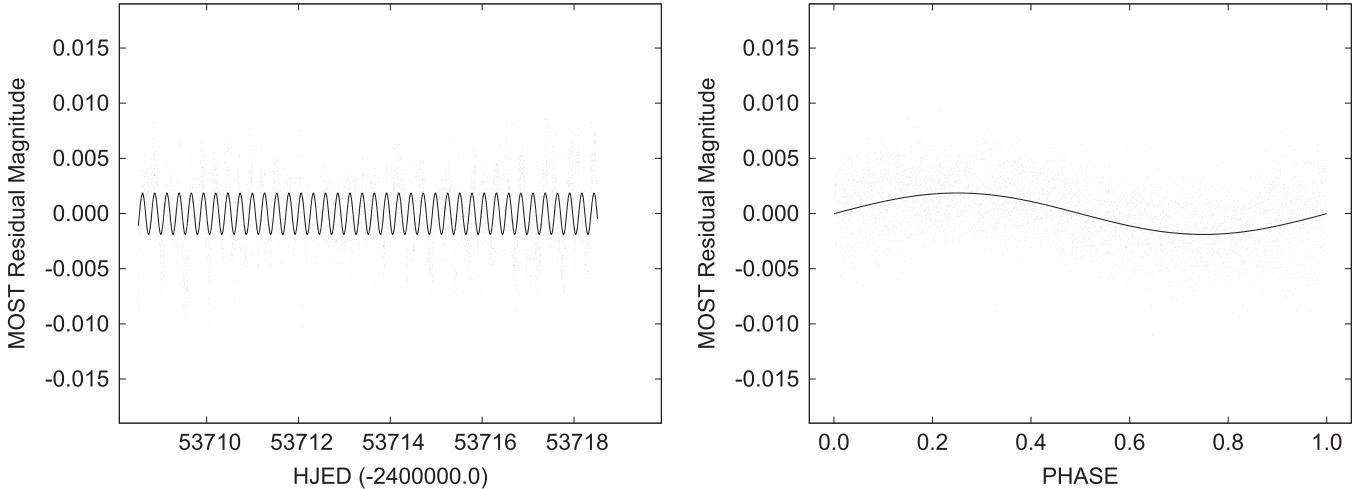
Figure 25. Same as Figure 24, but for a period of 0.256040 days. (This figure may not appear optimally in some browsers, resulting in missing data points).
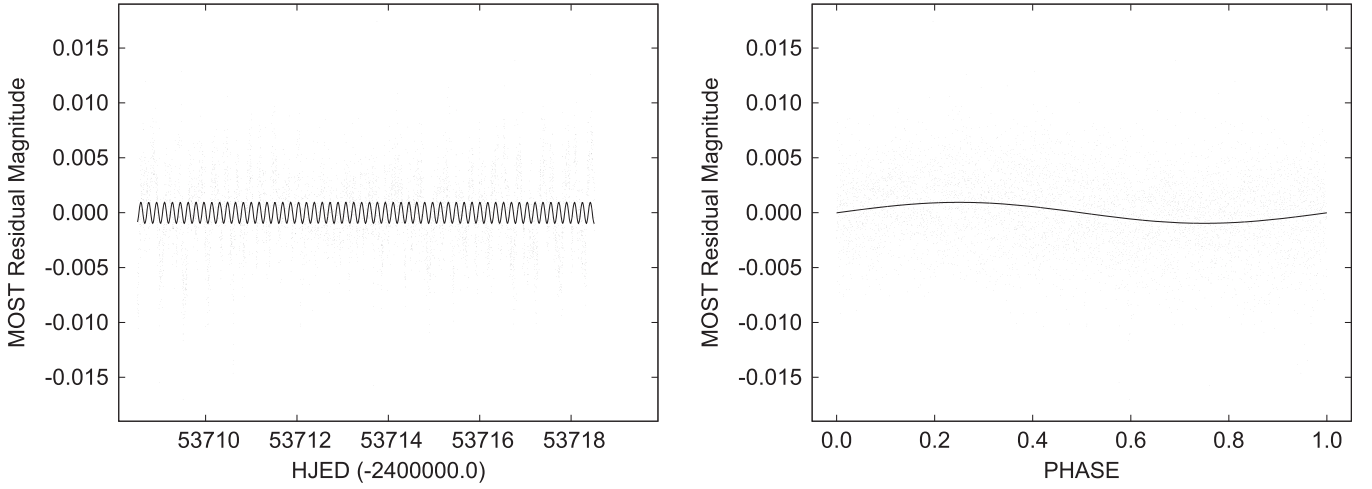
21

Figure 26. Same as Figure 24, but for detected periodicity 0.172546 days, nearly one-third the orbit period. (This figure may not appear optimally in some browsers, resulting in missing data points).
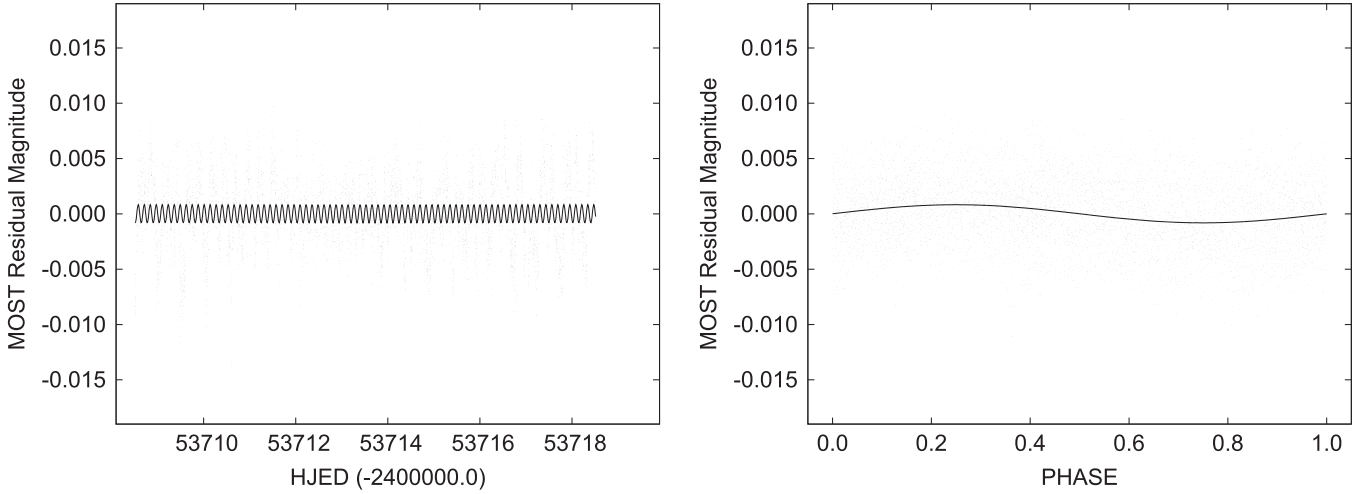

Figure 27. Same as Figure 24, but for detected periodicity 0.130151 days, nearly one-fourth the orbit period. (This figure may not appear optimally in some browsers, resulting in missing data points).
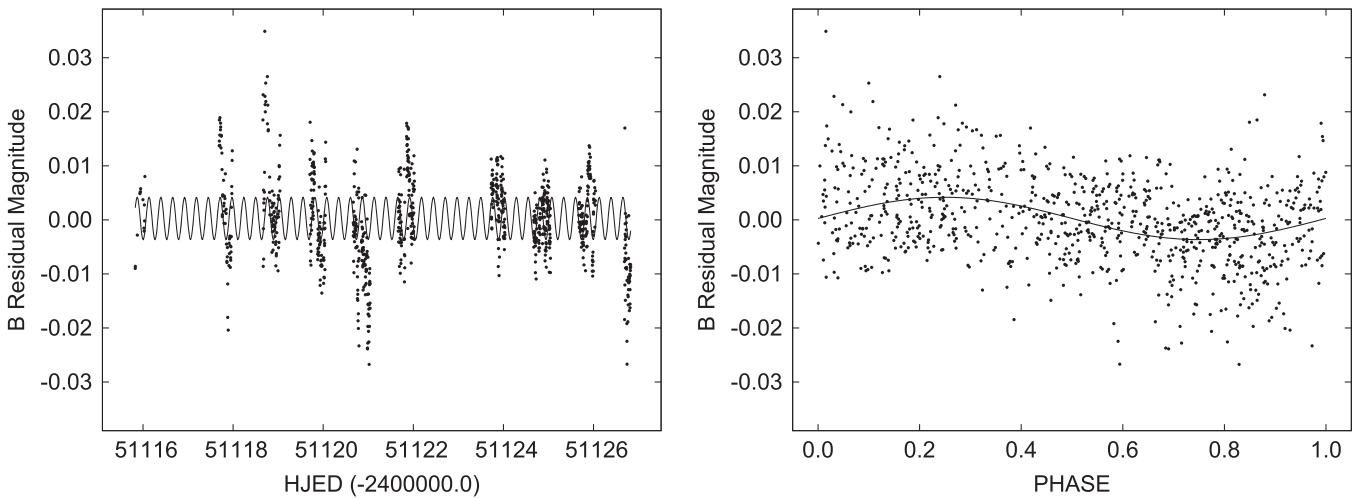

Figure 28. *B* residual magnitude and fitted 0.26294 day period sinusoid, close to half the orbit period.

adjust, together with parameters *a*, V_γ, and ephemeris zero-epoch, T_0. The results (Table 16) do not agree with those in Hussain et al. (2006) or Kaminski et al. (2007). Our RV-only

solutions find zero eccentricity within its uncertainty from the Kaminski et al. data. The Hussain et al. RVs give a small nonzero *e*.
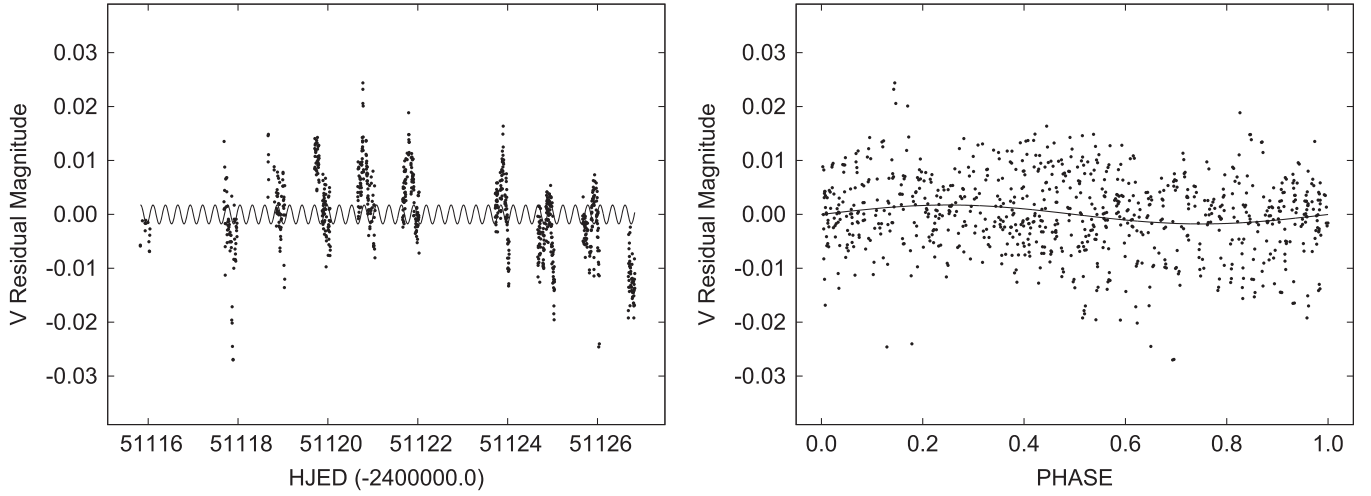
Figure 29. Same as Figure 28, but for *V* band and period of 0.27644 days.
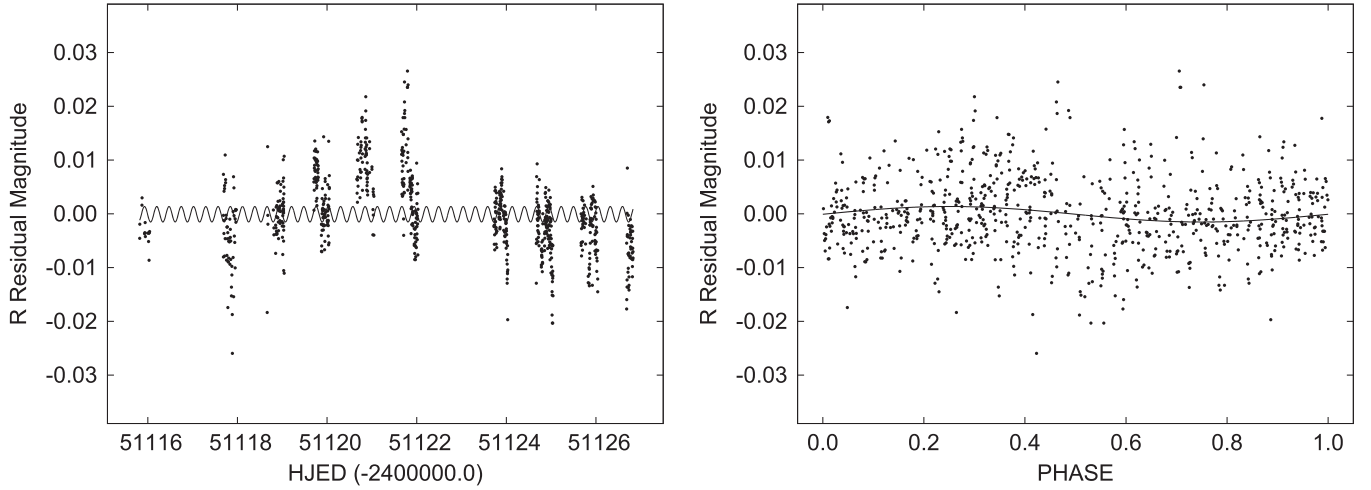
Figure 30. Same as Figure 28, but for R_C band and period of 0.2734 days.
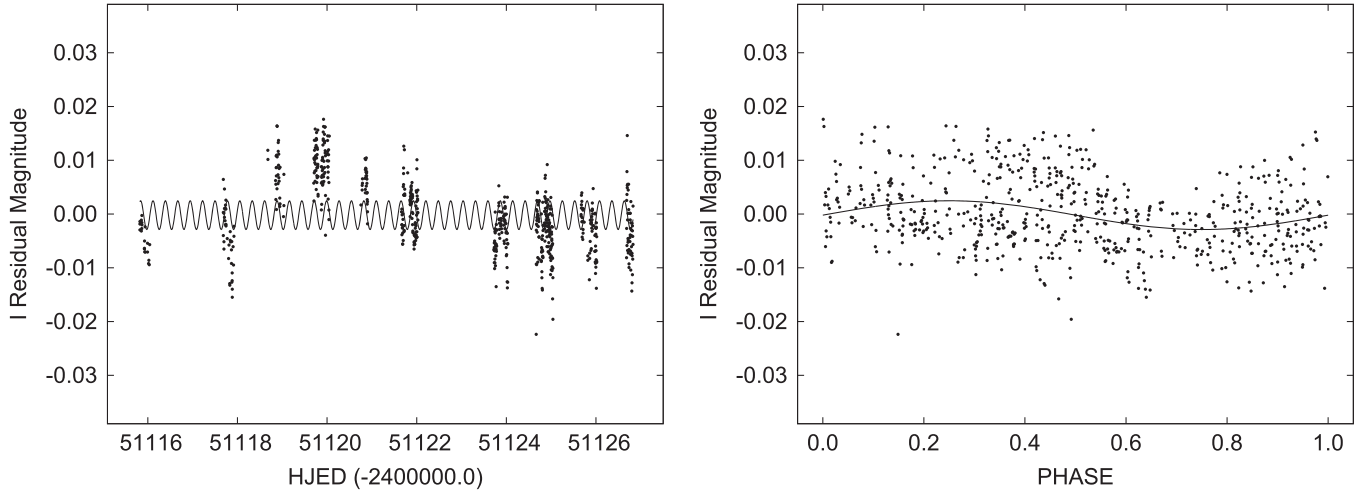
Figure 31. Same as Figure 28, but for I_C band and period of 0.27675 days.

9. ON THE REALITY OF THE THIRD STAR

9.1. Recent AO Results in Perspective

Long-standing and widespread acceptance of a 3b light-time effect as the cause of the apparent period variation has recently been challenged (Hardy et al. 2015) by means of AO observations in the photometric *H* band made on 2014 December 11 that hopefully mark the beginning of imaging of the system's near field. Figure 3 of Hardy et al. contains a composite rendering of the field and a plot of estimated contrast
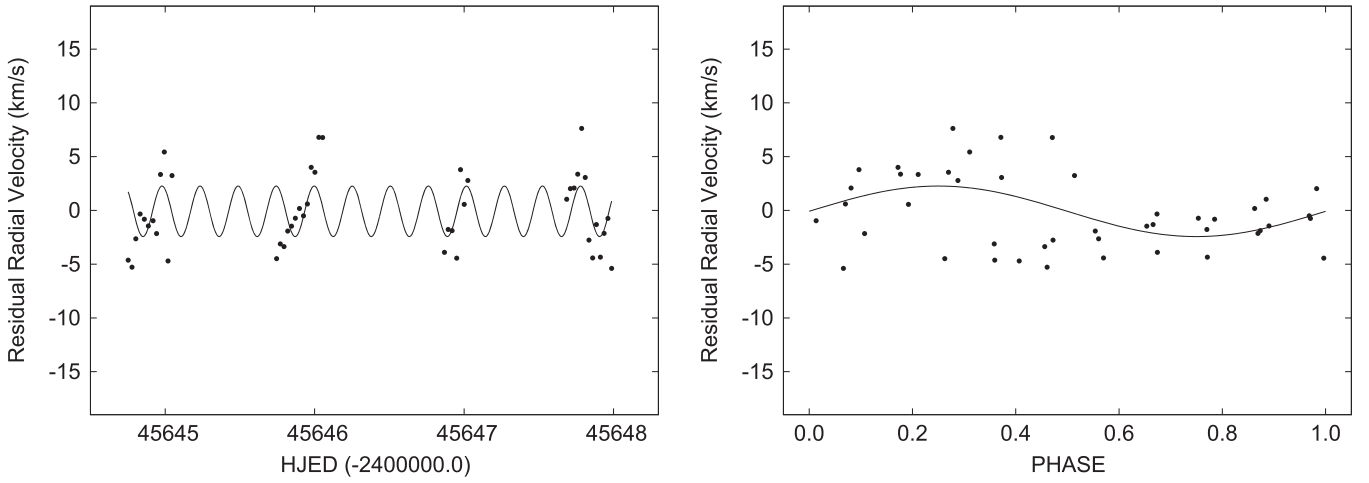
Figure 32. RV residuals (Bois et al. 1988) and fitted 0.2546 day period sinusoid, close to half the orbit period.
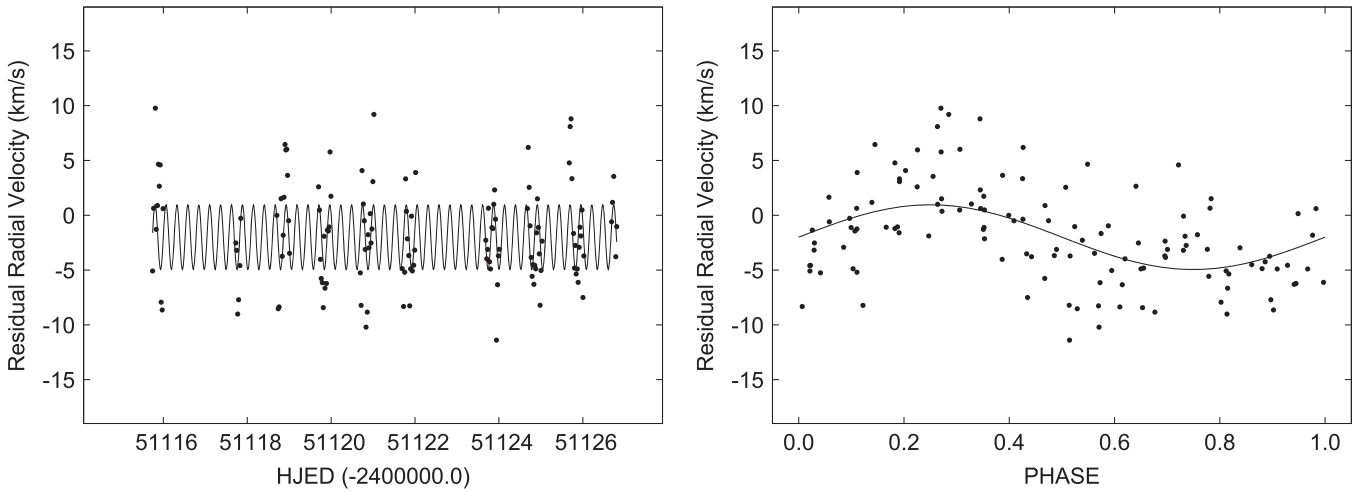
Figure 33. RV residuals (KPNO) and fitted 0.26029 day period sinusoid.
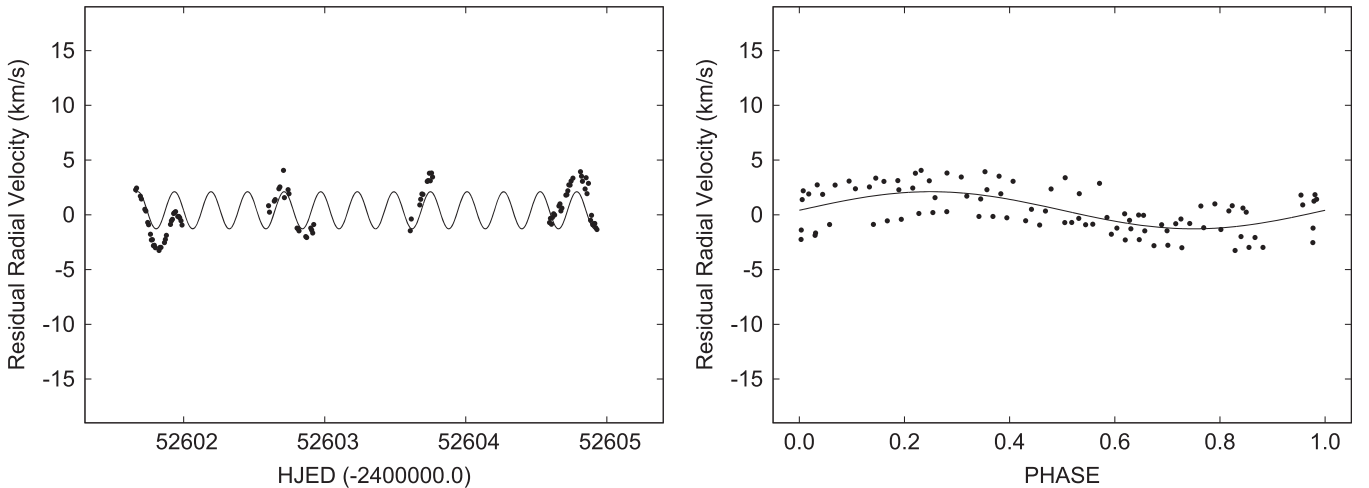
Figure 34. RV residuals (Hussain et al. 2006) and fitted 0.2593 day period sinusoid.

versus angular separation, where contrast means magnitude difference between the 3b and EB. The EB lies in the center of a circular ring of radius 260 mas, the Hardy et al. estimated separation for the date of the AO observation. The search area is a ring because the 3b's position angle cannot be determined

from light-time variations. The Hardy et al. separation estimate came from an analysis of eclipse timings—essentially the same timings analyzed here as one type of input to our unified light-RV-timing solutions. No obvious features are seen in their search ring, although there are a few barely visible wisps.

Table 16
Eccentric V471 Tau Red Dwarf Radial Velocity Solutions

Parameter	RVs from Hussain et al. (2006)	RVs from Kaminski et al. (2007)
a $(R_\odot)$	3.4692 ± 0.0026	3.437 ± 0.012
V_γ (km s^{-1})	37.28 ± 0.08	35.79 ± 0.34
e	0.00842 ± 0.00074	0.0019 ± 0.0031
ω (radians)	5.273 ± 0.086	3.9 ± 1.6
T_0 (HJED $-$ 2445821.0)	0.90028 ± 0.00012	0.89831 ± 0.00029

Note. Other parameters were fixed at values for the "all-data, no-*MOST*, *MOST*-radii" solution (column 5 of Table 8).

Hardy et al. conclude that existence of the light-time 3b is disproved by their AO image, as they predict the 3b to be at least 3 mag above their computed marginal detection level. As we are now armed with the most comprehensive and thoroughly checked set of analytic results ever assembled on V471 Tau, based not only on eclipse timings but on those timings plus nine light curves and six RV curves, the predicted EB to 3b separation and H-band magnitude difference can be newly computed. The key issues will now be examined.

9.2. The 3b Minimum Mass and Maximum Age

Categories for the prospective 3b other than brown dwarf clearly seem ruled out, as lower-mass categories are eliminated by the minimum-mass estimates in several papers, while ordinary stars of even the lowest masses would have been discovered easily. A compact exotic object in a very low inclination orbit may not be excluded with complete certainty, but can be excluded realistically. At issue with respect to detectability is the estimated faint limit for an observationally determined minimum 3b mass.

Brown dwarf bandpass luminosities increase with mass and decrease with age, with some dependence on metallicity and surface gravity, so predicted minimum luminosity mainly follows from estimates of minimum mass and maximum age. Our minimum mass of 0.0350 ± 0.0005 $M_\odot$ in Table 10 that corresponds to $i_{3b} = 90°$ is 20% lower than the Hardy et al. value of 0.044 ± 0.001 $M_\odot$. H-band luminosity depends steeply on mass, so the difference in minimum mass is significant. Maximum plausible age for the 3b is that of the Hyades cluster, which has typically been taken to be about 625 Myr, although recent contributions (Brandt & Huang 2015a, 2015b) have estimated about 800 Myr after including rotation in evolutionary models. Accordingly, Table 17 gives 3b minus EB magnitude differences (δH indicates contrast) for both ages, based on tables of brown dwarf models at the website of F. Allard.[15] A descriptive review paper is Allard et al. (2012). The results for ages 625 and 800 Myr are $\delta H = 9.65$ and 9.96 mag, respectively, making the brown dwarf about 0.5 and 0.8 mag fainter than estimated by Hardy et al. (2015), and thus closer to the marginal detection level by those amounts, although still respectively about 2.4 and 2.1 mag above the Hardy et al. detection limit for the 260 mas search ring. A possible reason for the difference in minimum mass (Hardy et al. versus here) is that Hardy et al. adopted the OBBS masses that are based on the Bois et al.

(1988) RVs that give outlier masses among results from the five red dwarf RV curves. All red star RV curves except the one used by OBBS, including the much more precise RVs from Kaminski et al. (2007) and from Hussain et al. (2006), give higher masses for both EB components.

9.3. A Binary Brown Dwarf?

A plausible circumstance not mentioned by Hardy et al. is that the 3b may be a *pair* of brown dwarfs that could be much fainter than one brown dwarf with the total mass of the little binary. Such a binary is not hard to believe, given the well-known theoretical difficulties of forming single stars and the existence of hierarchical multiple-star systems. Table 17 therefore also gives δH for examples of such a pair (two 0.0175 $M_\odot$ brown dwarfs) extracted from the Allard tables. The δH then becomes 11.21 mag at 625 Myr and 11.71 mag at 800 Myr, which places them about 0.9 and 0.4 mag above marginal detection in Hardy et al.'s Figure 3. So even in this case the object could perhaps be seen, assuming that the Hardy et al. marginal AO detection curve is accurate, although with a margin as little as 0.4 mag rather than the 3.0 mag by Hardy et al. or our 2.1 mag margin estimate for the case of one brown dwarf. However, the solution outcome with most potential consequences comes next.

9.4. The Angular Separation on 2014 December 11

The account up to this point is of two sets of brightness estimates (Hardy et al. and here) that roughly agree (within 0.8 mag) if the 3b is one brown dwarf but not if it is a binary of two equal brown dwarfs. Hardy et al. predict sure detection if the 3b exists, while this paper allows for less confident detection or perhaps nondetection if the 3b is really a binary of two brown dwarfs. The story now becomes more interesting—the object may have been seen.

Starting from the hypothesis that a 3b is responsible for the ≈ 30 yr periodicity via a light-time effect, as did Hardy et al., we computed the 3b-EB sky separation versus time, based on three of the solutions in Table 8 (all data, all data except *MOST* light curve, and timing-only solutions). The observational input had three kinds of precision-based weights according to precepts in Section 3.1. Representative sky path and angular separation (versus time) curves are shown in Figure 17, while separation on the date of the Hardy et al. AO observing is shown versus the (unknown) outer orbit inclination in Figure 18. Since none of the three data types convey information on the 3b orbit's rotational state about the line of sight, the position angle of the ascending node was set arbitrarily to $\pi/2$ rad, clockwise from north. In plane-of-sky rectangular coordinates, angular EB-3b displacements[16] in

---

[15] http://perso.ens-lyon.fr/france.allard/

[16] The displacements are referenced to the orbit's focus, as in usual practice, rather than to its center, as in the often-adopted work by Irwin (1952, 1959) on the light-time effect. That is why an unnecessary term in $e \cos \omega_{3b}$ is absent from our displacement equations and our light-time equation lacks the term in $e \sin \omega_{3b}$ seen in Irwin's papers and in papers that cite his work. This "center versus focus" distinction also explains why V471 Tau light-time plots in Ibanoglu et al. (1994), Guinan & Ribas, and Hardy et al. extend equally above and below zero for an eccentric orbit whose major axis is not in the plane of the sky. Maximum excursions above and below zero light-time, with respect to the system barycenter, are necessarily unequal for such an orbit.

Table 17
Estimated Brown Dwarf (BD) Magnitude Limits and Related Quantities

$M/M_\odot$	$T_{\rm eff}$ (K)	$R/R_\odot$	$\log_{10} g$ (cgs)	Surface m_H	m_H (49 pc)	$M_H({\rm BD}) - M_H({\rm EB})$
			Age 625 Myr			
0.0350	1325	0.0984	4.992	−34.730	16.99	9.65
$2 \times 0.0175^{\rm a}$	812	0.1042	4.640	−32.296	18.54	11.21
			Age 800 Myr			
0.0350	1221	0.0963	5.010	−34.461	17.30	9.96
$2 \times 0.0175^{\rm a}$	751	0.1027	4.655	−31.820	19.05	11.71

Note.
[a] The third body is a binary of equal-mass objects with a total mass of 0.0350 $M_\odot$.

arcseconds are

$$\delta_y = \frac{a_{3b}\cos(\upsilon_{3b}+\omega_{3b})\left(1-e_{3b}^2\right)}{(1+e_{3b}\cos\upsilon_{3b})d_{\rm pc}}, \qquad (4)$$

and

$$\delta_z = \frac{a_{3b}\cos i_{3b}\sin(\upsilon_{3b}+\omega_{3b})\left(1-e_{3b}^2\right)}{(1+e_{3b}\cos\upsilon_{3b})d_{\rm pc}}. \qquad (5)$$

Quantities υ_{3b} and ω_{3b} are, respectively, the true anomaly and argument of periastron in the outer (3b) orbit. The semimajor axis of the outer relative orbit, a_{3b}, is in AU, and $d_{\rm pc}$ is the system's distance in parsecs, for which 49 pc was adopted, as that is the mean of distances from our several solutions. It is nearly the same distance adopted by Hardy et al. (50 pc).

Our estimates of the angular separation $\delta_\rho = (\delta_y^2 + \delta_z^2)^{1/2}$ at the date of the Hardy et al. observation, obtained from Equations (4) and (5), differ from those of Hardy et al., likely owing to differing orbit parameters. Our values for e_{3b}, ω_{3b}, $a_{3b}\sin i_{3b}$, P_{3b}, dP/dt, and T_{03b} (time of superior conjunction of the 3b) are in Table 8. Those by Hardy et al. are not yet in print, to our knowledge, so a discussion of reasons for differences between this paper's predicted sky separation and that by Hardy et al. cannot be in terms of parameter results but only in terms of the quantity, precision, and variety of the basic input data, in concert with applied analysis strategies.

9.5. Why a Different Estimate of Angular Separation Now?

Without knowing the input parameter values for the Hardy et al. separation calculation, one cannot be sure of the reason or reasons for our different result. The difference may arise as a result of the overall comprehensiveness of our solutions, whose input has information from all previous eclipse timings, including the four recent Hardy et al. points, and also from all published light curves and RV curves. It has been done in various data combinations in addition to the all-data solution (see Table 8) so as to explore possible systematic variations among data sets. We have not just relied on the enormously weighty *MOST* data (57,000+ points) being fully satisfactory, but have experimented with various combinations, some of which exclude *MOST*. All such solutions except all-data give a ring radius about 80% of that of Hardy et al., who analyzed the same eclipse timings, although not any light curves or RV curves. The all-data ring is even smaller.

A specific reason for the difference in predicted separation could be our inclusion of dP/dt as a solution parameter, while Hardy et al. assumed that $dP/dt = 0$. Table 8 shows that the dimensionless dP/dt is nonzero and a 25σ result, consistently over Table 8's five solutions, with a value of $+0.295 \pm 0.012 \times 10^{-10}$ for the all-data solution. Indeed, we reproduce the Hardy et al. prediction of about 260 mas for 2014 December 11 if we do a timing-only solution with $dP/dt = 0$ and apply the resulting parameters to a calculation of projected sky motion, which suggests that most of the difference in separation may be due to our allowance for period change, which has not been done in previous V471 Tau papers. This outcome is surprising, as the small dP/dt integrates to phase differences of only about 0.00343 cycles, or 2.6 minutes of time, over the 40 yr of timings, so the match with the Hardy et al. computed separation in the no-dP/dt case may be a coincidence, although it is suggestive. A likely cause of the slow period increase is transfer of angular momentum from white dwarf spin to the orbit via magnetic coupling. The white dwarf is in fast rotation with a period of 9.25 minutes (Jensen et al. 1986; Robinson et al. 1988; Stanghellini et al. 1990; Barstow et al. 1992, 1997; Clemens et al. 1992; Sion 1992; Wheatley 1998).

9.6. Could the 3b Have Already Been Seen?

The proposed 3b would have passed the point of maximum projected separation and made a good start toward minimum separation when the AO observations were made. From our timing-only solution (for most direct comparison with Hardy et al.) we find $\approx$207 mas separation for that date, with small variations according to which of our solutions is applied, but essentially predicting a radius for the search ring about 80% of that by Hardy et al. (2015). This reduction in ring radius is a game changer for two crucial reasons. One is that the AO detection limit is a magnitude brighter for the smaller ring (see Figure 3 of Hardy et al.), so our former 2.4 mag margin for detection of a 0.0350 $M_\odot$ brown dwarf at 625 Myr age becomes 1.4 mag, and the 2.1 mag detection margin at 800 Myr becomes 1.1 mag. For the binary brown dwarf at 625 and 800 Myr the respective margins drop from 0.9 and 0.4 mag to negative (i.e., undetectable) values of −0.1 and −0.6 mag. The second crucial reason is that features *are* seen within the smaller ring, for example, strong ones at about 4 and 10 o'clock. So Hardy et al. may actually have discovered the 3b. Of course, continued imaging observations that look for Keplerian motion, so as to distinguish real star-like objects from artifacts of the contrast enhancement process, will be needed to check on this

possibility. Success would tell the position angle of the ascending node and have a definite measurement of the 3b orbit inclination and thus also the 3b mass rather than only mass as a function of inclination.

9.7. The 30 yr Waveform

The timing diagram (Figure 16, left panel) has translational symmetry—a shift of about 30 yr brings the two maxima essentially into register. The symmetry *could* result from three discontinuous period changes of about the same magnitude, alternate sign, and equal spacings—but would require matched behavior at three epochs, which seems unlikely. A 3b light-time effect represents the eclipse timings well, apart from two relatively small dips, although full consensus on the existence of the third star from timing data may require further timings over several decades or more, as periodicity needs to be established for a slowly varying phenomenon.

The light-time waveform agrees with Keplerian motion over 1.3 cycles, for the most part. We do not see the two brief dips as a serious concern, since few timing diagrams lack some irregularity, as can be seen by examining those in Kreiner et al. (2001). Hardy et al. (2015) suggest a magnetic phenomenon (Applegate 1992) that has no waveform prediction except that the form can change from cycle to cycle (i.e., that there is no definite waveform) and therefore the phenomenon cannot be tested from timing variations.

Our bottom-line estimate of the minimum margin for detection of the light-time 3b is $+0.4$ mag if it is one brown dwarf and -0.6 mag if it is a pair of equal brown dwarfs of the same total mass, where negative margins correspond to nondetectability. Of course, these are minimum estimates, showing that the 3b *could have escaped* detection, although the 3b could be much brighter and may already have appeared in the AO observation, as noted in Section 9.6.

Confirmed detection may come from further AO observations that look for a feature in Keplerian motion, or from other direct imaging (speckle?, above-atmosphere?) with one or more large telescopes, as proposed by Guinan & Ribas (2001) and now begun by Hardy et al. (2015). With good estimates of the object's minimum brightness and its angular separation from the EB along with deep images, a positive outcome is likely if the object exists and would bring closure to a controversy of long standing.

REFERENCES

Alexander, M. E., Chau, W. Y., & Henriksen, R. N. 1976, ApJ, 204, 879
Allard, F., Homeier, D., & Freytag, B. 2012, RSPTA, 370, 2765
Applegate, J. H. 1992, ApJ, 385, 621
Barstow, M. A., Holberg, J. B., Cruise, A. M., & Penny, A. J. 1997, MNRAS, 290, 505
Barstow, M. A., Schmitt, J. H. M. M., Clemens, J. C., et al. 1992, MNRAS, 255, 369
Bastian, U. 2000, IBVS, 4822, 1
Beach, T. E. 1985, IBVS, 2670, 1
Beavers, W. I., Herczeg, T. J., & Lui, A. 1986, ApJ, 300, 785
Bois, B., Lanning, H. H., & Mochnacki, S. W. 1988, AJ, 96, 157
Bois, B., Lanning, H. H., & Mochnacki, S. W. 1991, AJ, 102, 2079
Bond, H. E., Schaefer, K. G., Sion, E. M., Saffer, R. A., & Cheng, F. H. 1999, in ASP Conf. Ser 169, 11th European Workshop on White Dwarfs, ed. J. E. Solheim & E. G. Meištas (San Francisco, CA: ASP), 360
Brandt, T. D., & Huang, C. X. 2015a, ApJ, 807, 58
Brandt, T. D., & Huang, C. X. 2015b, ApJ, 807, 24
Cester, B., & Pucillo, M. 1976, A&A, 46, 197
Chatzopoulos, E., Robinson, E. L., & Wheeler, J. C. 2012, ApJ, 755, 95
Chau, W. Y., Henriksen, R. N., & Alexander, M. E. 1974, BAAS, 6, 488
Clemens, J. C., Nather, R. E., Winget, D. E., et al. 1992, ApJ, 391, 773
de Bruijne, J. H. J., Hoogerwerf, R., & de Zeeuw, P. T. 2001, A&A, 367, 111
Delandtsheer, A. C. 1983, Ap&SS, 92, 231
Eitter, J. J. 1987, IBVS, 3095, 1
Gallaudet, C., & Robinson, M. S. 2012, The Astronomical Almanac for the Year 2013 (Washington, DC: GPO)
Garcia-Alvarez, D., Drake, J. J., Lin, L. L., Kashyap, V. L., & Ball, B. 2005, ApJ, 621, 1009
Gilmozzi, R., & Murdin, P. 1983, MNRAS, 202, 587
Guinan, E. F., & Ribas, I. 2001, ApJL, 546, L47
Guinan, E. F., & Sion, E. M. 1984, AJ, 89, 1252
Hardy, A., Schreiber, M. R., Parson, S. G., et al. 2015, ApJL, 800, L24
Herczeg, T. J. 1975, IBVS, 1076, 1
Hric, L., Kundra, E., & Dubovsky, P. 2011, CoSka, 41, 39
Hussain, G. A. J., Prieto, C. A., Saar, S. H., & Still, M. 2006, MNRAS, 367, 1699
Ibanoğlu, C., Evren, S., Taş, G., & Çakirli, Ö 2005, MNRAS, 360, 1077
Ibanoğlu, C., Keskin, V., Akan, M. C., Evren, S., & Tunca, Z. 1994, A&A, 281, 811
Irwin, J. B. 1952, ApJ, 116, 211
Irwin, J. B. 1959, AJ, 64, 149
Jensen, K. A., Swank, J. H., Petre, R., et al. 1986, ApJL, 309, L27
Kaminski, K. Z., Rucinski, S. M., Matthews, J. M., et al. 2007, AJ, 134, 1206
Kim, J. S., & Walter, F. M. 1998, in ASP Conf. Ser. 154, Cool Stars, Stellar Syastens and the Sun, ed. R. A. Donahue & J. A. Bookbinder (San Francisco, CA: ASP), 1431
Kreiner, J. M., Kim, C., & Nha, I. 2001, An Atlas of O–C Diagrams of Eclipsing Binary Stars (Krakow: Wydawnictwo Naukowe Akademii Pedagogicznej)
Levenberg, K. 1944, QJMAM, 2, 164
Lim, J., White, S. M., & Cully, S. L. 1996, ApJ, 461, 1009
Lomb, N. R. 1976, Ap&SS, 39, 447
Lucy, L. B., & Sweeney, M. A. 1971, AJ, 76, 544
Lucy, L. B., & Sweeney, M. A. 1973, Obs, 93, 37
Marquardt, D. W. 1963, J. Soc. Indust. Applied Math, 11, 431
Martin, E. L., Pavlenko, Y., & Rebolo, R. 1997, ApJ, 326, 731
Miranda, V., Vaccaro, T., & Oswalt, T. D. 2007, JSARA, 1, 17
Mullan, D. J., Sion, E. M., Bruhweiler, F. C., & Carpenter, K. G. 1989, ApJL, 339, L33
Nelson, B., & Young, A. 1970, PASP, 82, 699
Nelson, B., & Young, A. 1976, in IAU Symp. 73, Structure and Evolution of Close Binary Systems, ed. P. Eggleton, S. Milton & J. Whelan (Dordrecht: Reidel), 141
Nicholls, J., & Storey, M. C. 1999, PASA, 16, 139
O'Brien, M. S., Bond, H. E., & Sion, E. M. 2001, ApJ, 563, 971 (OBBS)
Oliver, J. P., & Rucinski, S. M. 1978, IBVS, 1444, 1
Ostriker, J. P. 1976, in IAU Symp. 73, Structure and Evolution of Close Binary Systems (Cambridge), oral presentation
Paczynski, B. 1976, in IAU Symp. 73, Structure and Evolution of Close Binary Systems, ed. P. Eggleton, S. Milton & J. Whelan (Dordrecht: Reidel), 75
Parsons, S. G., Marsh, T. R., Gansicke, B. T., et al. 2012, MNRAS, 420, 3281
Pribulla, T., & Rucinski, S. M. 2006, AJ, 131, 2986
Ramseyer, T. F., Hatzes, A. P., & Jablonski, F. 1995, AJ, 110, 1364
Refsdal, S., Roth, M. L., & Weigert, A. 1974, A&A, 36, 113
Roberts, D. H., Lehár, J., & Dreher, J. W. 1987, AJ, 93, 968
Robinson, E. L., Clemens, J. C., & Hine, B. P. 1988, ApJL, 331, L29
Rucinski, S. 1979, AcA, 29, 203
Rucinski, S. M. 1981, AcA, 31, 37

Rucinski, S. M. 1983, IBVS, 2269, 1
Rucinski, S. M., Pribulla, T., & van Kerkwijk, M. H. 2007, AJ, 134, 2353
Scargle, J. D. 1982, ApJ, 263, 835
Shimansky, V. V., Bikmaev, I. F., & Shimanskaya, N. N. 2011, Ap. Bull, 66, 449
Sion, E. M. 1992, Natur, 358, 545
Sion, E. M., Bond, H. E., Lindler, D., et al. 2012, ApJ, 751, 66
Sion, E. M., Bruhweiler, F. C., Mullan, F. C., & Carpenter, K. 1989, ApJL, 341, L17
Skillman, D. R., & Patterson, J. 1988, AJ, 96, 976
Sparks, W. M., & Stecher, T. P. 1974, ApJ, 188, 149
Stanghellini, L., Starrfield, S., & Cox, A. N. 1990, A&A, 233, L13
Still, M., & Hussain, G. 2003, ApJ, 597, 1059
Taam, R. E., Bodenheimer, P., & Ostriker, J. P. 1978, ApJ, 222, 269
Tunca, Z., Keskin, V., Evren, S., Ibanoǧlu, C., & Akan, M. C. 1993, A&A, 204, 297
Tunca, Z., Tümer, O., Kurutaç, M., & Ibanoǧlu, C. 1979, Ap&SS, 64, 421
Vaccaro, T. R., Terrell, D., & Wilson, R. E. 2010, in ASP Conf. Ser. 435, Binaries—Key to Comprehension of the Universe, ed. A. Prša & M. Zejda (San Francisco, CA: ASP), 89
Vaccaro, T. R., & Wilson, R. E. 2002, in ASP Conf. Ser. 279, Exotic Stars as Challenges to Evolution, ed. C. A. Tout & W. van Hamme (San Francisco, CA: ASP), 167

Vogt, S. S. 1987, CoLic, 27, 317
Vogt, S. S., Penrod, D., & Hatzes, A. P. 1987, ApJ, 321, 496
Walter, F. M. 2004, AN, 325, 241
Werner, K., & Rauch, T. 1997, A&A, 324, L25
Wheatley, P. J. 1998, MNRAS, 297, 1145
Wilson, R. E. 1979, ApJ, 234, 1054
Wilson, R. E. 1983, Ap&SS, 92, 229
Wilson, R. E. 1990, ApJ, 356, 613
Wilson, R. E. 2006, in ASP Conf. Ser. 349, Astrophysics of Variable Stars, ed. C. Sterken & C. Aerts (San Francisco, CA: ASP), 71
Wilson, R. E. 2008, ApJ, 672, 575
Wilson, R. E. 2012, AJ, 144, 73
Wilson, R. E., & Biermann, P. 1976, A&A, 48, 349
Wilson, R. E., & Devinney, E. J. 1971, ApJ, 166, 605
Wilson, R. E., & Raichur, H. 2011, MNRAS, 415, 596
Wilson, R. E., & Van Hamme, W. 2009, ApJ, 699, 118
Wilson, R. E., & Van Hamme, W. 2014, ApJ, 780, 151
Wilson, R. E., Van Hamme, W., & Terrell, D. 2010, ApJ, 723, 1469
Yilmaz, M., Bastürk, Ö, Alan, N., et al. 2009, IBVS, 5887, 1
Young, A. 1976, ApJ, 205, 182
Young, A., Klimke, A., Africano, J. L., et al. 1983, ApJ, 267, 655
Young, A., & Lanning, H. H. 1975, PASP, 87, 461
Zorotovic, M., & Schreiber, M. R. 2013, A&A, 549, A95